



## Research paper

## Numerical investigation of the vortex-induced vibration of a circular cylinder in oscillatory flow

Hongjun Zhu<sup>a,\*</sup>, Huifen Xu<sup>a</sup>, Bin Liu<sup>b,c</sup>, Jiawen Zhong<sup>a</sup><sup>a</sup> State Key Laboratory of Oil and Gas Reservoir Geology and Exploitation, Southwest Petroleum University, Chengdu, 610500, China<sup>b</sup> Faculty of Science, Agriculture and Engineering, Newcastle University, Newcastle Upon Tyne, NE1 7RU, UK<sup>c</sup> Newcastle Research and Innovation Institute, Newcastle University in Singapore, 609607, Singapore

## ARTICLE INFO

## ABSTRACT

**Keywords:**  
 Vortex-induced vibration  
 Circular cylinder  
 Oscillatory flow  
 Wake evolution

The two-degree-of-freedom (2-DOF) vortex-induced vibration (VIV) of a circular cylinder in oscillatory flow is numerically investigated in this work. The wake flow and vibration response are examined at a Reynolds number of 150 and three Keulegan-Carpenter numbers of 20, 30, and 50 in the range of reduced velocity from 3 to 16. It is found that the root-mean-squared lift coefficient first increases and then decreases, and tends to be stable with the increase of the reduced velocity. The minimum averaged pressure coefficients at different KCs number decrease with the increase of reduced velocity. The time-averaged pressure coefficient is 0 at the front and rear stagnation points, presenting V-shaped at  $0 \leq \alpha \leq 180^\circ$ . The evolution of vortices is associated with the vibration response of the cylinder as well as the oscillatory flow. The vortices in turn influence the subsequent vibration of the cylinder, contributing to the multiple frequencies. The streamwise dominant frequency is always equal to the oscillatory flow frequency, despite the existence of multiple frequencies. In contrast, the transverse vibration frequency follows closely the natural frequency of the cylinder.

## 1. Introduction

In offshore engineering, the wave-induced vibration of marine structures is typically modelled by subjecting the structure to an oscillatory flow. This approach simulates the periodic fluctuation in flow velocity and direction characteristic of waves. The study of oscillatory flow around elastically mounted cylinders is crucial for understanding and modeling a range of problems, from coastal engineering flows to large-scale oceanographic flows (An et al., 2015). Such analyses are pivotal in exploring the dynamics of cylindrical structures like Floating Production Storage and Offloading (FPSO) units, marine risers, etc. Vortex shedding in the wake of a circular cylinder in steady flow is observed when the Reynolds number ( $Re = U_{max}D/v$ , where  $U_{max}$  is the max of fluid velocity,  $D$  is the diameter of the cylinder and  $v$  is the kinematic viscosity of the fluid.) surpasses approximately 47 (Henderson, 1997; Jiang et al., 2016). In particular, for the oscillatory flow around a cylinder, a dimensionless parameter, Keulegan–Carpenter (KC =  $U_{max}T/D$ , where  $T$  is the period of the flow oscillation) number, is employed to characterize the oscillatory feature.

As early as 1979, Bearman and Currier, as the pioneers in the research of fluid-structure interaction, conducted intensive research on

the vortex-induced vibration (VIV) (Bearman and Currie, 1979). VIV is commonly the cause of significant delays of construction and failures in offshore structures. The VIV motions of towed and moored underwater platforms degrade the data-gathering performance of these systems. The practical significance of VIV has led to extensive fundamental studies. Many of those were discussed in the comprehensive reviews of Feng (1968), Williamson (1996), Williamson and Govardhan (2004), and Williamson and Govardhan (2008). Feng (1968) documented classic measurements of the VIV response of an elastically mounted cylinder. There are two amplitude branches, namely the "initial" branch and the "lower" branch, with a hysteretic transition between them. Khalak and Williamson (1997) extended that free vibration at low mass and damping is associated with the existence of an "upper" branch of high amplitude response, which appears between the "initial" and "lower" branches. The phenomenon of lock-in or synchronization (Williamson and Govardhan, 2004) traditionally means that the ratio  $f^* = f/f_n$  remains close to unity, where  $f$  is the vibration frequency and  $f_n$  is the natural frequency. The lock-in region corresponds to a large amplitude of the cylinder. The vortex shedding per cycle comprises single vortex (S) and vortex pairs (P), yielding patterns such as 2S (two single vortices are shed per cycle), 2P (two pairs of vortices are shed per cycle), and P +

\* Corresponding author.

E-mail address: [zhuhj@swpu.edu.cn](mailto:zhuhj@swpu.edu.cn) (H. Zhu).

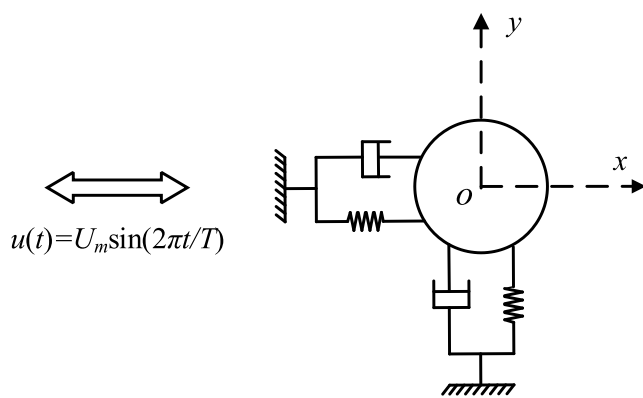


**Fig. 1.** Sketch of vortex induced vibration of a circular cylinder in oscillatory flow.

S (the cylinder sheds a pair of vortices and a single vortex per cycle) modes. Through the smoke visualizations, [Brika and Laneville \(1999\)](#) found that the "initial" and "lower" branches correspond to the 2S and 2P modes, respectively. Williamson and Govardhan summarized the vortex modes as 2S, 2P, 2T (three vortices in the same sign are shed in every half-period) and C(2S) (two vortices in the same sign but in different sizes are shed on both sides of the cylinder per cycle) modes ([Williamson and Govardhan, 2004](#)). New wake modes are subsequently found behind the oscillating structure, such as P + S ([Singh and Mittal, 2005](#)) and some combined ones.

In the actual marine environment, the relative oscillatory flow between the riser and the fluid driven by the wave and the top platform motion also leads to VIV. Under oscillatory flow conditions, the flow around the cylinder is very complicated. For different KC and Re, the vortical structure and vibration mechanism are different. [Sarpkaya \(1986\)](#) experimentally studied the flow around a cylinder in oscillatory flow. For a single cylinder at  $\beta = 730$  (where  $\beta$  is the Stokes number, defined as  $\beta = \text{Re}/\text{KC}$ ), the number of vortices shed from both sides of

the cylinder increases with the increase of KC number. Five vortex patterns were observed: attached vortex pair mode ( $0 < \text{KC} < 7$ ), one vortex pair mode ( $7 < \text{KC} < 15$ ), two vortex pairs mode ( $15 < \text{KC} < 24$ ), three vortex pairs mode ( $24 < \text{KC} < 32$ ), and four vortex pairs mode ( $32 < \text{KC} < 40$ ). Sarpkaya also found that when  $\text{KC} < 1.1$ , no vortex shed occurred, presenting the two-dimensional characteristics. When  $1.1 < \text{KC} < 1.6$ , the vortex shedding occurs ([Honji, 1981](#)). When  $1.6 < \text{KC} < 4$ , a pair of symmetric vortices are generated in half a period of oscillation. However, when  $4 < \text{KC} < 7$ , the turbulence phenomenon is intensified in the boundary layer, and a pair of asymmetric vortices are generated in half a period. When the KC number continues increasing, the number of vortices in a period increases. Subsequently, [Tatsuno and Bearman \(1990\)](#) conducted an experimental study on the visualization of flow around a cylinder in oscillatory flow ( $5 < \beta < 160$ ,  $1.6 < \text{KC} < 15$ ) and identified eight different regimes. In addition, [Sumer and Fredsøe \(1988\)](#), and [Kozakiewicz et al. \(1992, 1994, 1997\)](#) studied the characteristics of VIV of cylinder and riser in oscillatory flow via experimental methods, and found an intermittent transition of vibration mode. At a given KC number, the vibration of the cylinder changes with the velocity, and a prominent feature of the oscillatory flow is the co-existence of multiple peaks. With the increase of the KC number, the number of vorticity and the number of response peaks in a period increase, and the relevant parameters increase when the KC number is in the lock-in region. The position of the vortex shedding distance from the cylinder is affected by the vibration frequency of the cylinder.

The topic of oscillatory flow around a circular cylinder can be examined through different setups of coordinate systems. In most of the experiments, the cylinder was under an oscillatory motion in still water, where the coordinate system was fixed with far-field ([Elston et al., 2006](#); [Lam et al., 2010](#); [Williamson, 1985](#)), the Eulerian description. In numerical simulations, it is more convenient to simulate an oscillating flow past a stationary cylinder ([Justesen, 1991](#); [Obasaju et al., 1988](#); [Tatsuno and Bearman, 1990](#), etc.) instead, where the coordinate system was fixed with the cylinder, the Lagrangian description. In recent years, a lot of studies on mooring systems have been carried out by establishing a rigid cylinder model for experiments or numerical simulation. Considering the feasibility of the study, the six degrees of freedom of the

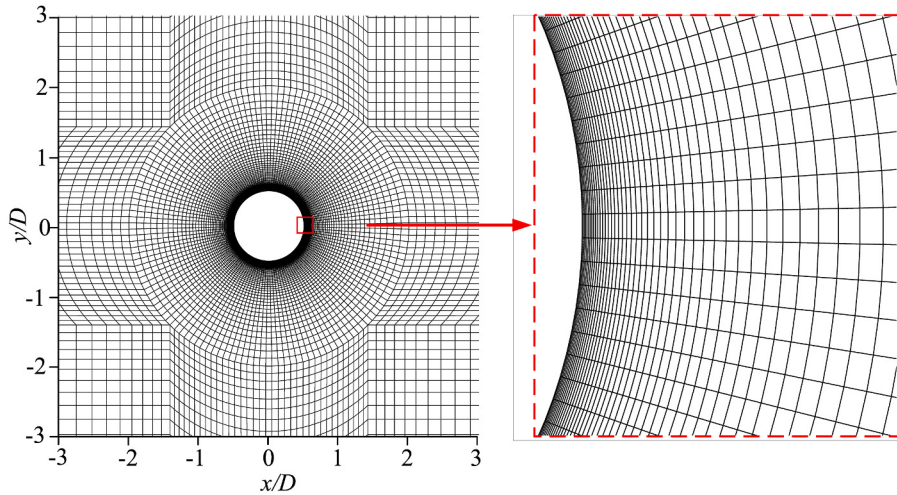
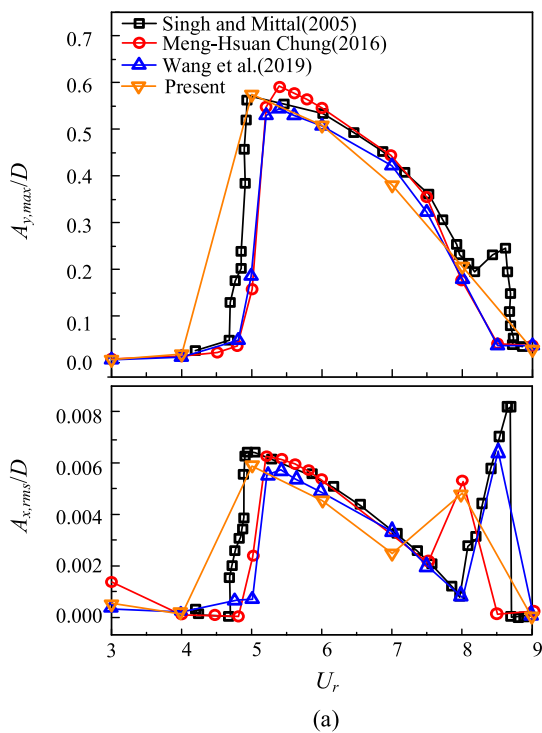


**Fig. 2.** Two-dimensional computational mesh near the cylinder.

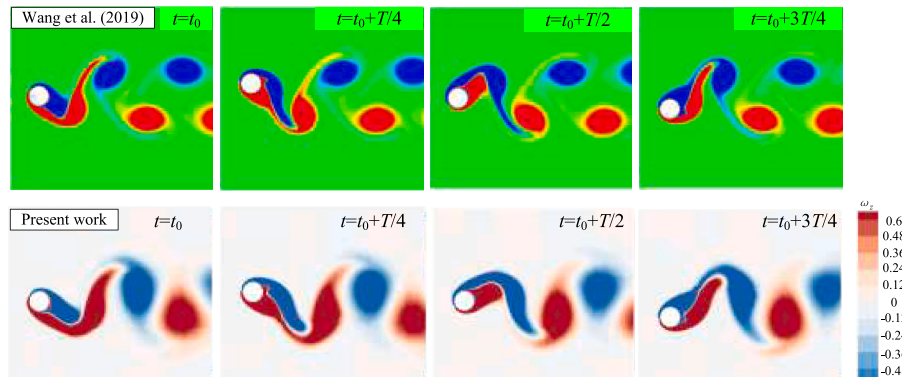
**Table 1**

Results for mesh dependency validation at  $\text{Re} = 150$ ,  $m^* = 2$ ,  $U_r = 5$ ,  $\zeta = 0$ , and  $\Delta r = 0.001$ .

Mesh	Element	$R_r$	$N_c$	$C_{D,\text{mean}}$	$C_{L,\text{rms}}$	$St$	$A_{x,\text{max}}$	$A_{y,\text{max}}$	$f^*$
M1	39169	1.1	25	0.4051	0.1789	0.2001	0.5159	0.9133	0.2001
M2	62455	1.07	30	0.4300 (6.15 %)	0.1814 (1.40 %)	0.2001 (0.00 %)	0.5438 (5.40 %)	0.9131 (0.02 %)	0.2001 (0.00 %)
M3	134317	1.05	40	0.4269 (-0.72%)	0.1807 (-0.51 %)	0.2001 (0.00 %)	0.5408 (-0.55 %)	0.9270 (1.50 %)	0.2000 (0.05 %)



(a)



(b)

**Fig. 3.** The comparison in the steady flow (a) the comparison of the amplitude of two-degree-of-freedom (2-DOF) VIVs with the results in the literature; (b) the comparison of the vortex shedding with that reported in [Wang et al. \(2019\)](#).

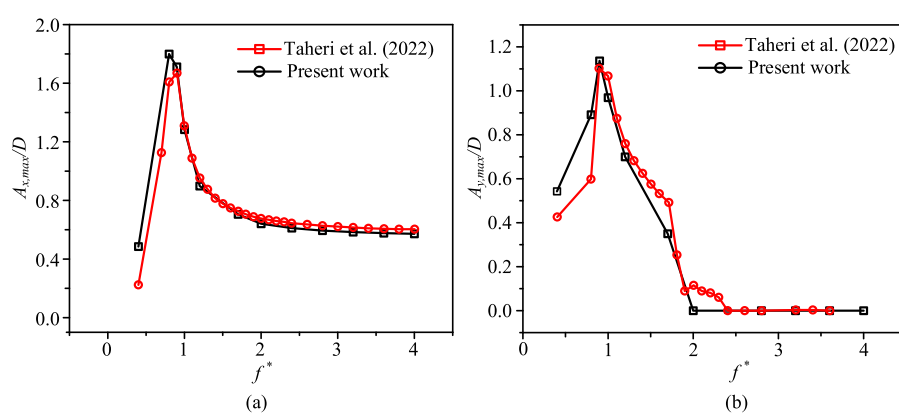


**Fig. 4.** The comparison of the maximum amplitudes with reported data: (a) in the streamwise direction; (b) in the transverse direction.

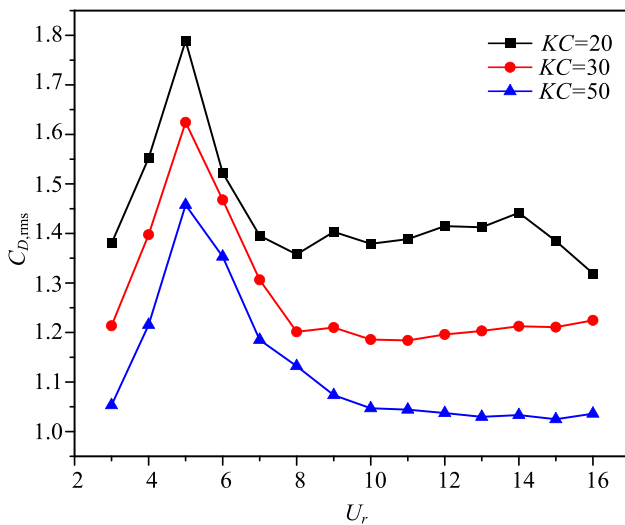


Fig. 5. The variation of root-mean-squared (RMS) drag coefficient with reduced velocity.

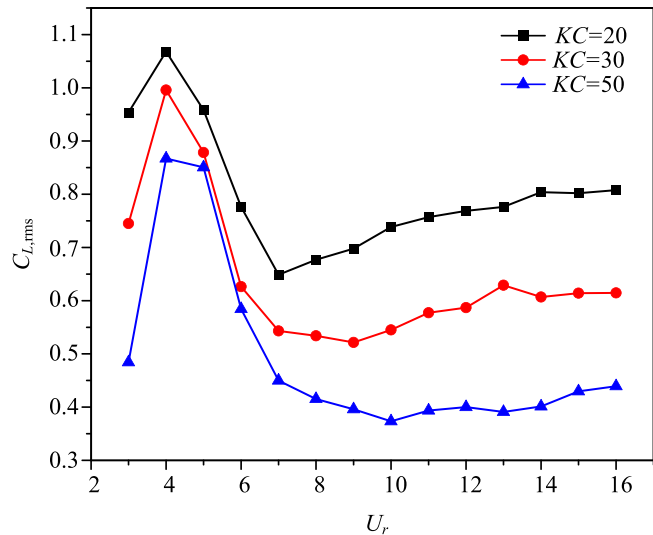


Fig. 6. The variation of root-mean-squared (RMS) lift coefficient with reduced velocity.

moving cylinder are simplified into one (transverse vibration) or two degrees of freedom (streamwise and transverse vibration). Physical model experiments and numerical simulation experiments of vortex-induced vibration of rigid cylinders can be divided into the following two categories: (1) Forced oscillation: vibration according to a specific function trajectory, the vibration trajectory is a mathematical function set by humans, is a specific vibration trajectory, will not change with the actual force of the cylinder, and the driving force is the external drive. (2) Self-excited oscillation: the oscillation of the cylinder is caused by the force generated when the fluid flows around, and the spontaneous motion generated under the excitation of the force. Self-excited vibration is a kind of spontaneous motion under the action of force, and the motion path is not artificially set in advance but is an autonomous movement under the action of fluid force. (3) Free vibration: The vibration in which the system is no longer stimulated after the initial excitation. (4) Parametric vibration: Vibration induced by changes in the system's parameters. Self-excited vibration is more intuitive than forced vibration, in the past few decades, the motion and force of

self-excited cylinders have been studied by many researchers. Sarpkaya (2004) described in his study that studying vortex-induced vibration to predict the motion and dynamics of self-excited oscillation based on the physical model of forced oscillation or numerical simulations. Conversely, the physical model of self-excited oscillation or numerical simulations can be used to predict the forced oscillation of the lift, drag, additional mass force coefficient, etc. Up to now, the primary focus of advanced experimental techniques is on the fluid-structure coupling between rigid cylinders and three-dimensional separation flows. In the experiment, the original six degrees of freedom of movement of the rigid cylinder was also simplified to one degree of freedom, namely the most concerned lateral movement. Both self-excited oscillation and forced oscillation experiments have their significance. The researchers can choose different experimental methods according to the objectives of their study. Nowadays, a lot of scientific research work has been carried out on the forced vibration and vortex-induced vibration of cylinders. The review papers published by Pan et al. (2005) provide a good summary of the studies in the past. In addition, studies on the correlation between forced vibration and vortex-induced vibration can be found in Morse and Williamson (2006), Hover et al. (2004), and Carberry et al. (2004, 2005). The experiments of forced vibration are of great significance. The experiments of forced vibration pay more attention to the energy transfer between fluid and structure motion. Among them, Staubli (1983), Moe and Wu (1990), and Gopalkrishnan (1993) have attracted more attention. Among them, Sarpkaya decomposed the fluid force suffered by the cylinder in forced oscillation into components that are in phase with the cylinder oscillation velocity, that is, the drag force component, and the inertial force component that is in phase with the oscillation acceleration. After this decomposition, although it is not as intuitive as that considered in the self-excited oscillation experiment, it clearly expresses the role of vibration frequency in energy transfer. Patrikalakis and Chryssostomidis (1986) give the lift response of a cylinder under shear flow in one direction. The data from Gopalkrishnan's experiment were adopted by the lift model of vortex-excited vibration software Shear7.

It was noticed that there are very limited studies on the vibration of cylinders in an oscillating flow. Kozaiewicz et al. (1994, 1997) conducted an experimental study of 1-DoF (degree of freedom) vibration of a cylinder in the oscillating flow direction for  $5 < KC < 100$ . It was found that the response mode under constant KC number changes with the reduced velocity. One of the typical characteristics of the response in an oscillating flow is that the frequency of the vibration is a multiple of the frequency of the oscillating flow. Sumer et al. (1994) studied the streamwise correlation of a vibrating cylinder in an oscillating flow, and the large amplitude of oscillation at the resonance has a significant effect on the flow pattern and the hydrodynamic force exerted on the cylinder. Anagnostopoulos and Iliadis (1998) numerically simulated the directional vibration of a cylinder in an oscillating flow with  $Re = 200$  and KC number between 2 and 20. It is found that the large oscillation amplitude at the resonance has a great influence on the flow pattern and the hydrodynamic force exerted on the cylinder. Zhao et al. (2012, 2013) conducted study on 1-DoF VIV of a cylinder in the transverse direction of oscillating flow and showed that the numerical model based on the Reynolds-averaged Navier-Stokes equations can well predict the vortex-induced vibration patterns observed in laboratory. Lipsett and Williamson (1994) conducted laboratory tests in a U-tube to study the XY trajectory of vibrations by changing the KC number from 2 to 60 and the ratio of the natural frequency in water to the U-tube oscillation frequency from 1 to 9. Zhao (2013) also conducted a 2dof numerical study on cylindrical vortex-induced vibration affected by oscillating flow. It can be observed that as the KC number increases, the vibration becomes irregular and chaotic as the vibration amplitude increases.

Overall, it was found that most studies on oscillating flows focused on high Reynolds number, and few studies on low Reynolds number oscillating flows. and the description of the outcome after vortex shedding is lacking. In this study, the two-degree-of-freedom vortex-induced

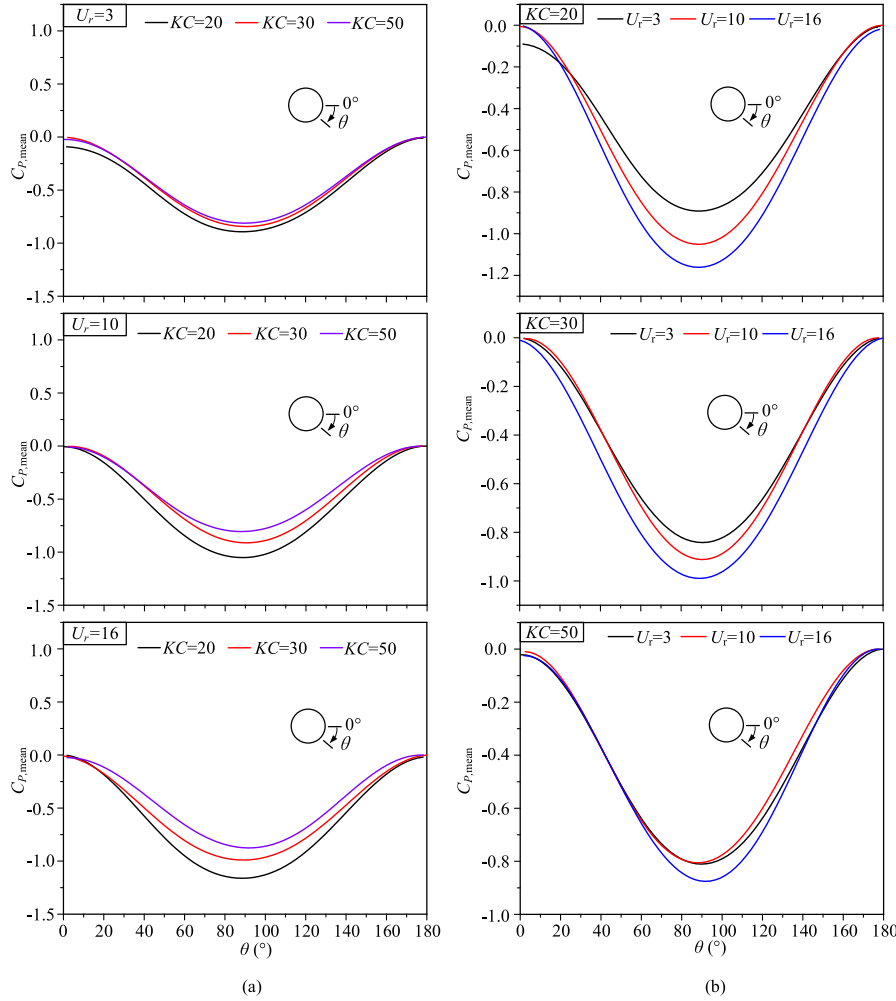


**Fig. 7.** The distribution of the mean pressure coefficient ( $C_{P,\text{mean}}$ ) around the cylinder: (a) comparison of different KCs number at the constant reduced velocity; (b) comparison between different reduced velocity at the constant KC number.

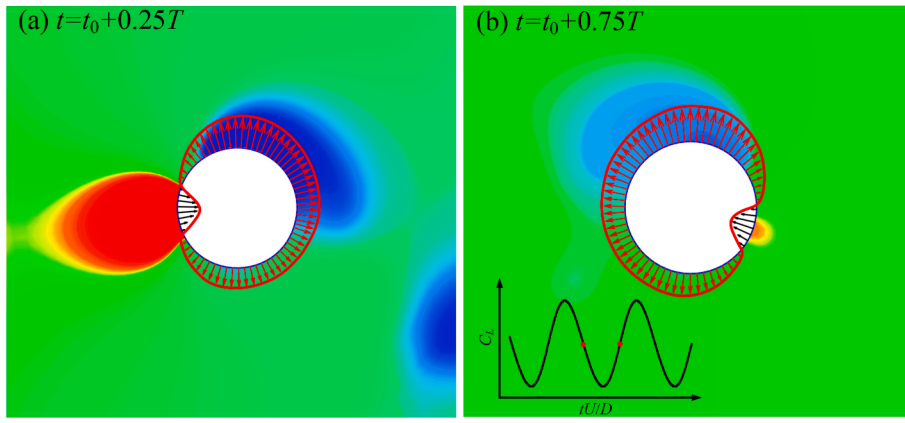


**Fig. 8.** Pressure coefficient contours at two moments when  $KC = 20$  and  $U_r = 3$ : (a)  $t = t_0 + 0.25T$ ; (b)  $t = t_0 + 0.75T$ .

vibration response of a cylinder in oscillating flow at low  $Re$  was numerically investigated, including vibration displacement in two directions of the cylinder, lift and drag force, and vortex shedding of the cylinder wake, etc., and the reduced velocity  $U_r$  from 3 to 16,  $Re = 150$ ,  $m^* = 10$ , and damping ratio equal to zero. However, in practical engineering, the period of waves usually ranges from 0.5 to 25 s with flow velocity in the range of 0.5–1.5 m/s, and the size of marine structures

varies from as small as 0.2 m (e.g. subsea pipelines) to as large as 90 m (e.g. floating production storage and offloading, FPSO). The value of KC roughly ranges from 0.003 to 200. Therefore, in this work, three typical KC values ( $KC = 20, 30$ , and  $50$ ) are selected within the range. The relationship between the cylinder amplitude and hydrodynamic coefficient and the reduced velocity under different KCs number was studied, and the relationship between vibration frequency and flow mode was

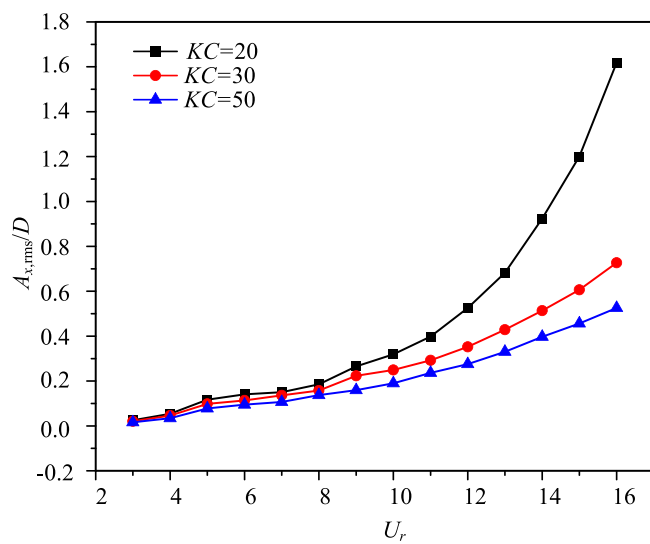


Fig. 9. The variation of root-mean-squared (RMS) amplitude in the streamwise direction with the reduced velocity.

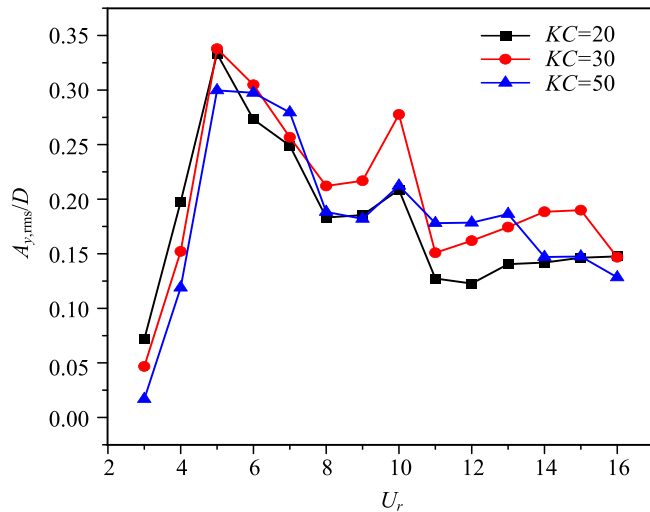


Fig. 10. The variation of root-mean-squared (RMS) transverse amplitudes with reduced velocity.

studied by observing the eddy current movement around the cylinder.

The structure of this article is arranged as follows. In Section 2, the governing equations and numerical models used in this study are presented, and the numerical model is validated by comparing the numerical results with the experimental test results. In Section 3, three KCs number  $KC = 20, 30, 50$ , and  $U_r = 3\text{--}16$  are simulated to discuss the relationship between the vibration response of the reduction speed to the cylinder and the hydrodynamic system values for different KCs number. Conclusions are drawn in section 4.

## 2. Numerical method

### 2.1. Governing equations

Two-dimensional numerical simulations were executed using the open-source Computational-Fluid-Dynamics (CFD) solver OpenFOAM ([www.openfoam.org](http://www.openfoam.org)), which is composed of C++ libraries solving the continuity and incompressible Navier-Stokes (NS) equations (1) and (2)

directly by the finite-volume method (FVM) and the Pressure Implicit with Splitting of Operators (PISO) algorithm,

$$\frac{\partial u_i}{\partial x_i} = 0 \quad (1)$$

$$\frac{\partial u_i}{\partial t} + u_j \frac{\partial u_i}{\partial x_j} = -\frac{1}{\rho} \frac{\partial p}{\partial x_i} + \nu \frac{\partial^2 u_i}{\partial x_i \partial x_j} \quad (2)$$

where  $(x_i, x_j) = (x, y)$  are the Cartesian coordinates in the streamwise and transverse directions, respectively,  $u_i$  is the velocity component in the  $x_i$  direction,  $t$  is time,  $p$  is pressure,  $\rho$  and  $\nu$  are the density and kinematic viscosity of the fluid, respectively. The governing equations for the structure are given by:

$$M\ddot{X} + C\dot{X} + KX = F_D(t) \quad (3)$$

$$M\ddot{Y} + C\dot{Y} + KY = F_L(t) \quad (4)$$

where  $M$ ,  $C$  and  $K$  are the mass, damping and stiffness of each cylinder, respectively,  $\ddot{Y}$ ,  $\dot{Y}$  and  $Y$  represent the transverse acceleration, velocity and displacement, respectively;  $\ddot{X}$ ,  $\dot{X}$  and  $X$  represent the streamwise acceleration, velocity and displacement, respectively;  $F_L$ ,  $F_D$  are the lift force and the drag force acting on the cylinder, respectively.

Once the flow field is obtained, drag and lift coefficients can be defined as:

$$C_D = \frac{2F_D}{\rho U^2 D} \quad (5)$$

$$C_L = \frac{2F_L}{\rho U^2 D} \quad (6)$$

where  $C_D$  and  $C_L$  are the drag and lift coefficients, respectively.

### 2.2. Problem description and boundary conditions

Fig. 1 shows a sketch of the 2dof VIV of a circular cylinder in the oscillatory flow. The fluid velocity of the sinusoidally oscillatory flow  $u(t)$  is expressed as:

$$u(t) = U_m \sin(2\pi t / T) \quad (7)$$

where  $t$  is the time and  $T$  is the period of oscillation. The non-dimensional parameters that influence the VIV are: (1) the mass ratio  $m^* = m/m_d$ , where  $m$  is the mass of the cylinder and  $m_d$  is the mass of the displaced fluid ( $m_d = \rho\pi D^2 L/4$ ); (2) the structural damping ratio  $\zeta = C/(2\sqrt{Km})$ , where  $C$  is the structural damping constant and  $K$  is the stiffness of the spring; (3) the reduced velocity  $U_r = U_m/f_{nw} D$ , where  $f_{nw}$  is the natural frequency of the structure measured in still water, where  $f_{nw} = (1/2\pi)\sqrt{K/m}$  and  $K$  is the stiffness of spring; (4) the KC number  $KC = U_m T/D$  and (5) the Reynolds number  $Re = U_m D/\nu$ , where  $\nu$  is the kinematic viscosity of the fluid.

### 2.3. Spatial and temporal convergence analysis

The computational domain was structured using Gmsh with a refined grid distribution around the circular cylinder, as depicted in Fig. 2. The smallest normalized grid height near the cylinder surface is set to 0.001 $D$ . The grid refinement was performed within a circular region encompassing the cylinder to ensure accurate capture of the wake and vortex street behind the cylinder. Fig. 2 shows the close look of the mesh around a cylinder. The structured mesh near the cylinder's surface has been adequately refined to capture the boundary layer. The height of the first layer close to the cylinder surface is 0.001 $D$  (the smallest element size), and the time step  $dt = 0.001$  is used for all simulations in this article.

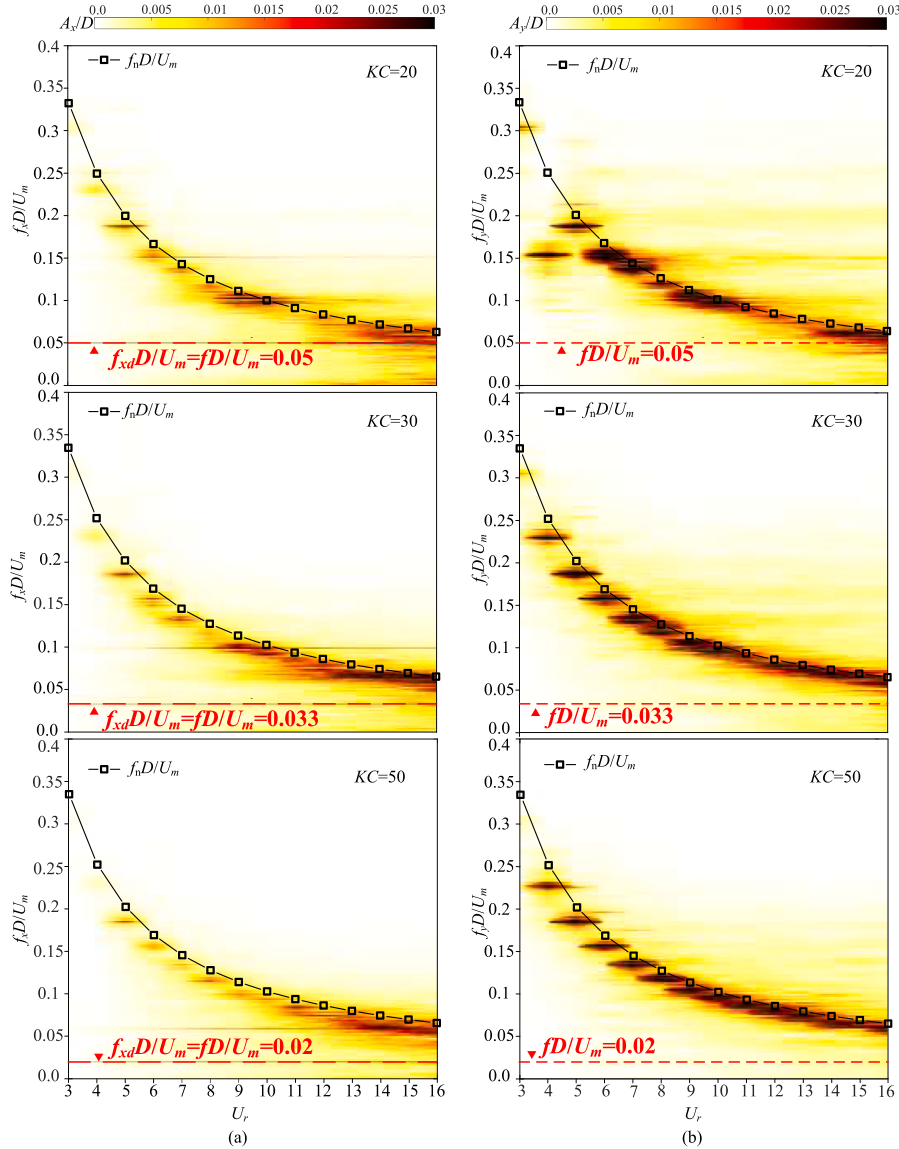


**Fig. 11.** Comparison of amplitude frequency and natural frequency of different KCs number: (a) in the streamwise direction; (b) in the transverse direction.

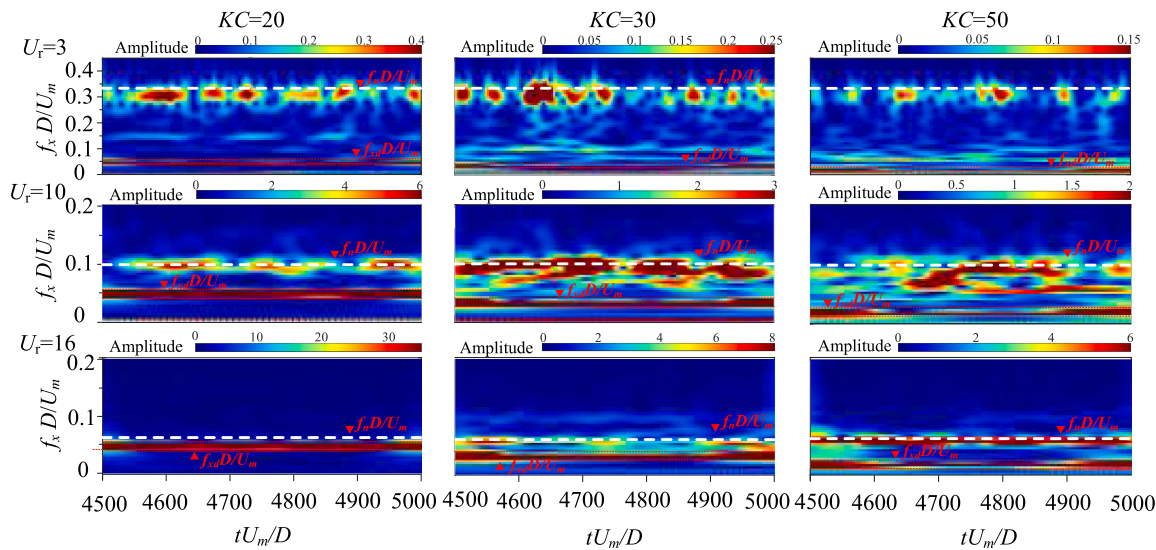


**Fig. 12.** Comparison of wavelet spectrum in streamwise direction with different KCs number and reduced velocity.

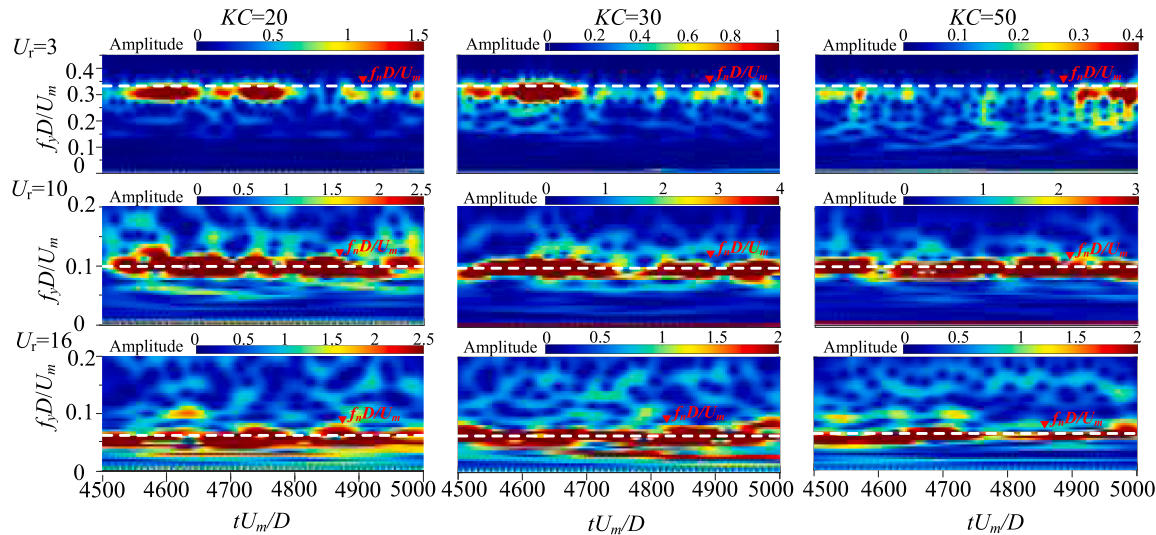


**Fig. 13.** Comparison of wavelet spectrum in the transverse direction with different KCs number and reduced velocity.

The mesh convergence analysis was conducted for the cylinder in steady flow when \$U\_r = 5\$. As is shown in Table 1, it is evident that the error of the hydrodynamic and vibration response is within 5% for the mesh resolution M2, where Element, \$R\_r\$, \$N\_c\$, \$C\_{D,\text{mean}}\$, \$C\_{L,\text{rms}}\$, \$St\$, \$A\_{x,\text{max}}\$, \$A\_{y,\text{max}}\$, are the total node number of the mesh, the radial growth rate, the number of circumferential nodes around the cylinder, the mean drag coefficient, root-mean-square of the lift coefficient, the Strouhal number, the maximum streamwise amplitude, the maximum transverse amplitude, and the frequency ratio (\$f^\* = f\_w/f\_n\$, where \$f\_w\$ is the oscillatory flow frequency and \$f\_n\$ is the natural frequency of the cylinder), respectively, and \$\Delta r\$ is the minimum non-dimensional mesh size. Hence, M2 is used for all simulations in this article. Note that the simulation of each case is carried out until enough periodic results are obtained after a statistically stable flow state has been reached.

#### 2.4. Code validation

Figs. 3 and 4 show the two-degree-of-freedom steady flow verification, and the maximum amplitude verification of oscillating flow

direction, respectively. Fig. 3 (a) is compared with Singh and Mittal (2005), Chung (2016), and Wang et al. (2019) respectively to compare the changes of the maximum transverse amplitude with the reduced velocity and the changes of the root-mean-squared (RMS) value of the streamwise amplitude with the reduced velocity. As shown in Fig. 3, the curve obtained by this model is similar to the corresponding curve in previous literature, and two peaks of \$A\_{x,\text{rms}}/D\$ curves similar to those of predecessors are also found in this work. The \$A\_{y,\text{max}}/D\$ in this paper are in good agreement with the results obtained by Chung (2016) and Wang et al. (2019). Fig. 3 (b) is the vorticity contours in the wake of a circular cylinder in one vortex shedding cycle are compared with that observed by Wang et al. (2019). It can be seen from Fig. 4 that the vortex shedding mode is in consistent with the reported literature, presenting the classical 2S mode. The difference in the transverse distance between vortices is possibly associated with the display range of vorticity contours, since the vorticity range is not provided in Wang et al. (2019).

Fig. 4 shows the comparison between the maximum streamwise amplitude calculated by the current model and the maximum streamwise direction amplitude calculated by the model used by Taheri et al.

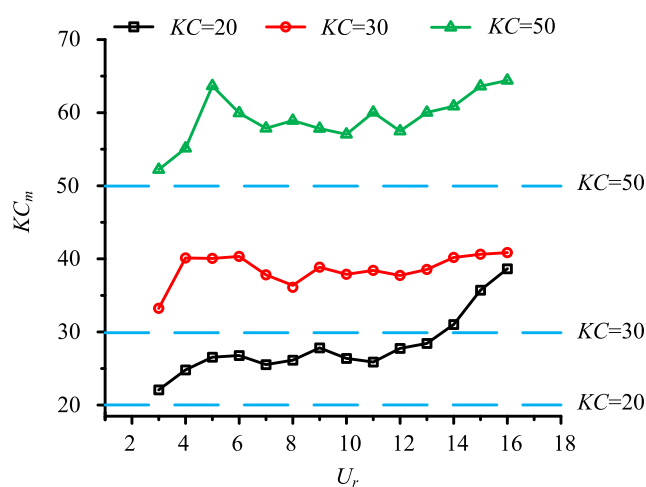


Fig. 14. Dependence of the maximum KC number on the reduced velocity.

(2020), the normalized velocity is defined as  $f^* = U_r/KC$ . Fig. 4 compares the maximum amplitudes in both streamwise and transverse directions. It is seen that the calculated results agree well with the reported data. Each set of calculations by Taheri et al. (2022) is for single degree of freedom, while the current validation is for two degrees of freedom. Thus, there are differences in some reduced velocities.

### 3. Results and discussion

#### 3.1. Hydrodynamic coefficients

Figs. 5 and 6 show the variation of the root-mean-square (RMS) force coefficient with the reduced velocity. For each KC number, the variations of the RMS streamwise and the RMS transverse force coefficients with the reduced velocity are characterized by rapidly increasing to a peak followed by gradually decreasing and then stable with the increase of reduced velocity. The variation of the root mean square (RMS) force coefficient is similar to the changes of the transverse amplitude with the reduced velocity.

As depicted in Fig. 5, the root-mean-square value of the drag coefficient gradually increases when  $3 < U_r < 15$ . Conversely, it decreases when  $5 < U_r < 8$ , and tends to stabilize when  $8 < U_r < 16$ . Moreover, the stability of the curve improves with the KC number increases. Additionally,  $C_{D,\text{rms}}$  decrease progressively with increasing KC number at a constant reduced velocity, due to a longer oscillation period resulting in a greater time required for velocity direction changes.

As shown in Fig. 6, the root-mean-square value of the lift coefficient gradually increases when  $U_r = 3$  and  $U_r = 4$ , and the root-mean-square value of the lift coefficient decreases in proportion when  $5 < U_r < 7$ , while the root-mean-square value of the lift coefficient increases slightly when  $8 < U_r < 16$ , and with the decrease of KC number, the root-mean-square value of the lift coefficient increases more and more significantly. At the same reduced velocity, the root-mean-square value of the lift coefficient also decreases with the increase of KC number, and because the oscillation period becomes larger, the time required to change the velocity direction becomes larger, resulting in the root-mean-square value of the drag coefficient decreases with the increase of KC number at the constant reduced velocity.

#### 3.2. Pressure coefficients distribution

Figs. 7 and 8 show the circumferential distribution curve of the averaged pressure coefficient for typical groups, and the circumferential distribution diagram of the instantaneous pressure coefficient at four moments in half a cycle before and after the velocity direction change when  $KC = 20$  and  $U_r = 3$ , respectively.

The time-averaged pressure is calculated with more than 100 oscillating flow cycles, and then the time-averaged pressure coefficient is obtained by:

$$C_{P,\text{mean}} = \frac{P_{\text{mean}} - P_{\infty}}{\frac{1}{2}\rho U_m^2} \quad (8)$$

where  $P_{\text{mean}}$  is the time-mean pressure, and  $P_{\infty}$  is the independent static pressure at the inlet. Fig. 7(a) shows the time-averaged pressure coefficient around the cylinder at different KCs number with a given reduced velocity.

Fig. 7 (a) shows the comparison between the mean pressure coefficients of oscillating and steady flows with different KCs number at the constant reduced velocity. The minimum averaged pressure coefficients of different KCs number will continue to decrease with the increase of reduced velocity, and the greater the reduced velocity, the more obvious the difference between the averaged pressure coefficients of the different KCs number. Due to the separation of the shear layer, the averaged pressure curve of each stage presents a V-shape in the range of  $0 \leq \alpha \leq 180^\circ$ . The mean circumferential pressure distribution of oscillating flow is obviously different from that of stable flow, because of the change of flow direction. Fig. 7 (b) shows the comparison between the averaged pressure coefficients of different reduced velocity in the constant KC number. It can be seen that the minimum value of the averaged pressure coefficient will gradually decrease with the increase of the reduced velocity, and the difference between the averaged pressure coefficient values of different reduced velocity will become smaller and

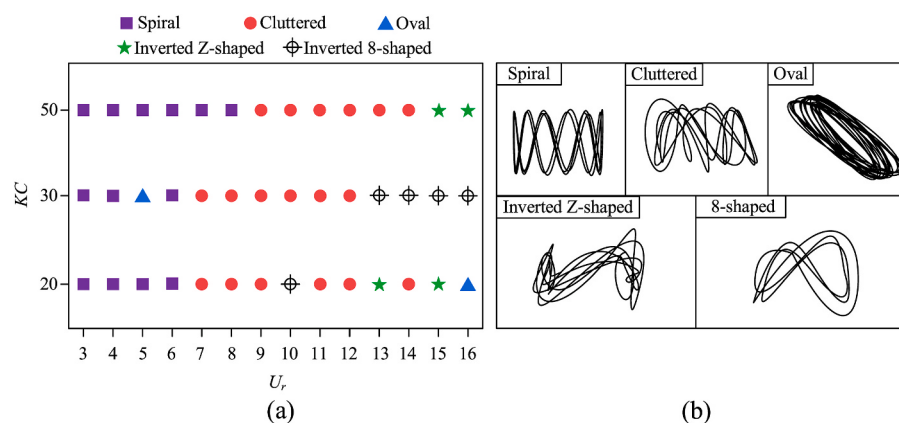
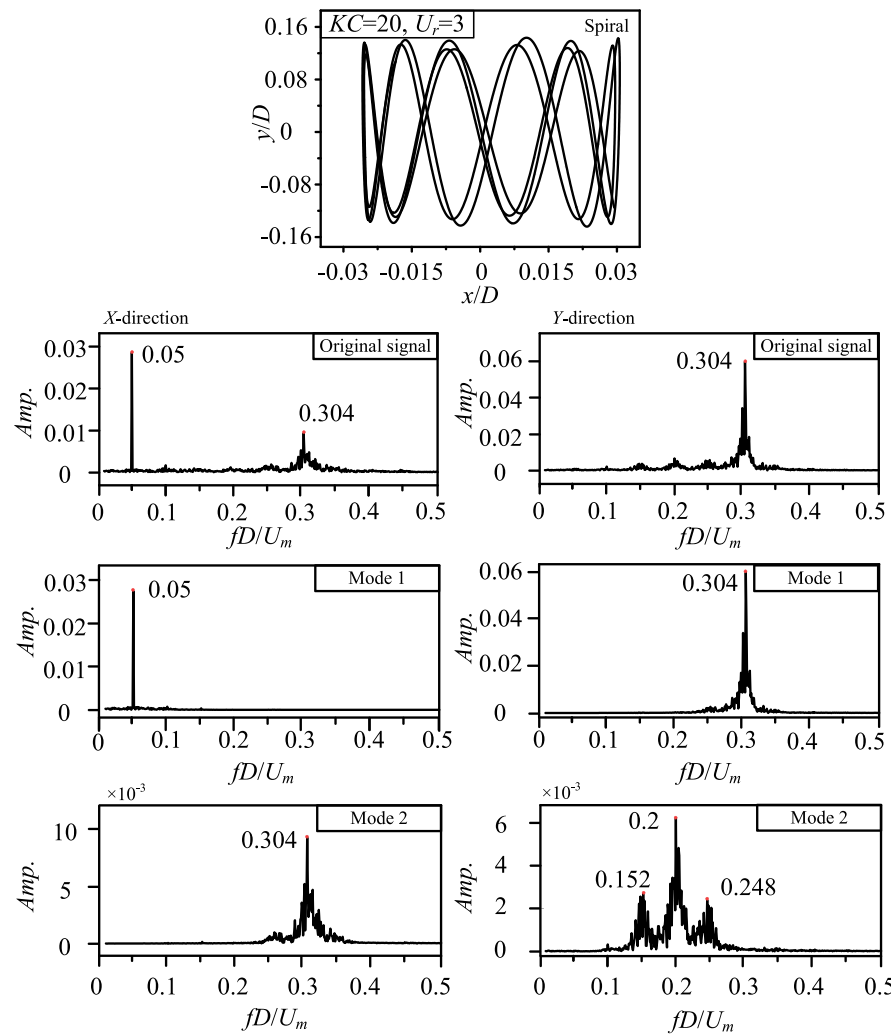


Fig. 15. The division of displacement trajectory pattern in the case considered in the current work: (a) displacement trajectory partition; (b) five typical shapes of trajectories.



**Fig. 16.** The displacement trajectory and the vibration frequency at  $KC = 20$ ,  $U_r = 3$ .

smaller, with the increase of the KC number.

In Fig. 8, the red arrow outward represents the negative pressure zone, and the black arrow inward represents the positive pressure zone. The pressure coefficient in half period of the oscillating flow is plotted in Fig. 8. The distribution of positive and negative pressure presents a center symmetry with the velocity change. From Fig. 8 (a) and Fig. 8 (b), it can be seen that the positive and negative pressure regions appearing in front and rear of the cylinder are approximately symmetrically distributed. With the switching of flow velocity direction, the positive and negative pressure regions on both sides of the cylinder exchange their positions. The shed vortices of the positive flow impact on the cylinder surface when the reverse flow occurs, influencing the flow velocity and hence the pressure. Therefore, the sizes of pressure regions have some differences. It can be concluded that the averaged pressure coefficient is 0 in the front and rear stagnation points of the cylinder, presenting a V-shape in the range of  $0 \leq \alpha \leq 180^\circ$  and a W-shape in the range of  $0 \leq \alpha \leq 360^\circ$ .

### 3.3. Vibration response

Figs. 9 and 10 show the streamwise and transverse amplitudes, respectively. As seen in Fig. 9, the larger the KC number, the smaller the streamwise amplitude. The cycle of oscillating flow becomes larger with the growth of KC number, contributing to more stable movement of the cylinder and hence the reduction of streamwise amplitude. In contrast,

the streamwise amplitude is enlarged with the increase of the reduced velocity, which is altered with the natural frequency in this work. The same phenomenon is observed by Zhao et al. (2013).

It can be seen from Fig. 10 that the root-mean-squared value of the transverse amplitude gradually increases when  $3 < U_r < 5$ , and the three KCs number show a trend of first decreasing and then increasing in the range of  $6 < U_r < 11$ ; in the range of  $5 < U_r < 16$ , there is an overall decreasing trend, which is similar to the lift coefficient. The transverse direction junction is similar to the experimental results in Kang et al. (2016) in that it increases first and then decreases in the reduced velocity range.

Fig. 11 illustrates the vibration frequencies at different KCs number and reduced velocity, where  $f_{xd}$  is the dominant frequency in the streamwise direction and the normalized oscillatory flow frequency is highlighted with red dashed line. It is seen that the dominant frequency in the streamwise direction is always equal to the oscillatory flow frequency, in spite of the existence of multiple frequencies. In contrast, the transverse vibration frequency follows closely the natural frequency of the cylinder. As a result, the vibration amplitude in the transverse direction is small, and the influence of vortices is not as significant as the streamwise direction.

Figs. 12 and 13 show the comparison between the streamwise and transverse wavelet contours and the natural frequency, respectively. And which verifies the statement of Fig. 11. The streamwise dominant frequency does not coincide with the natural frequency of the cylinder

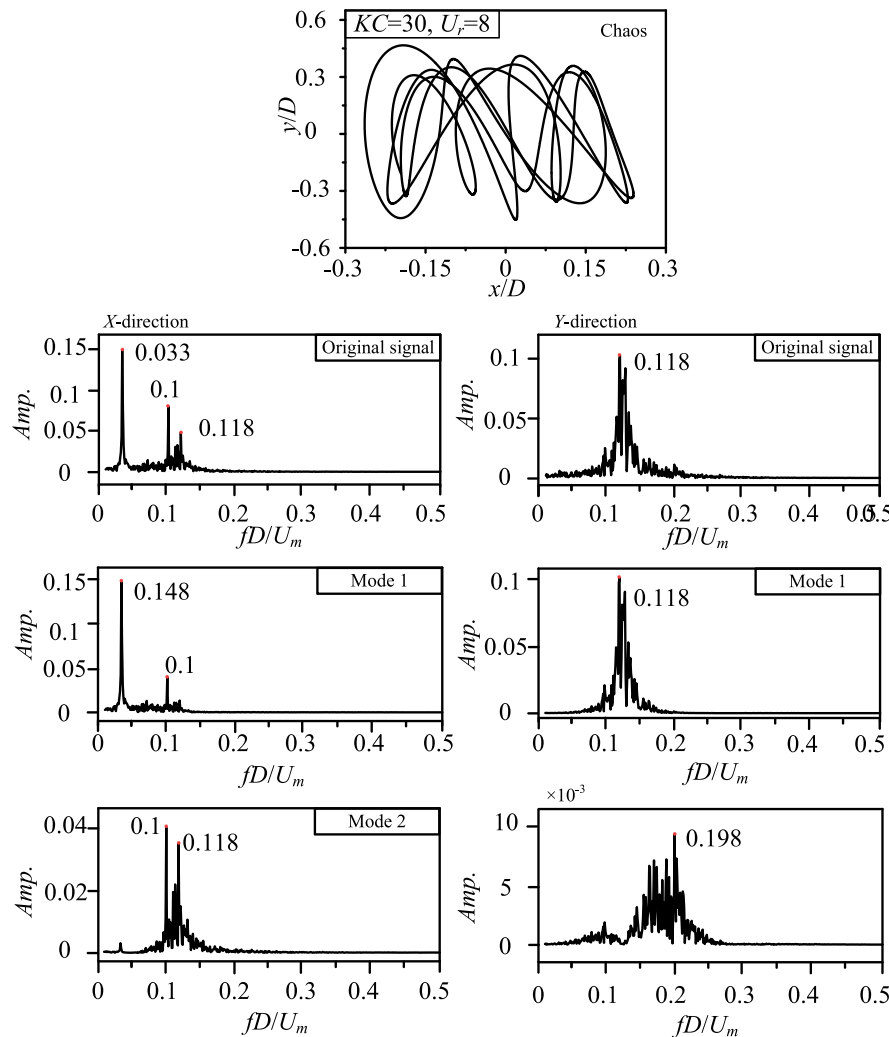


**Fig. 17.** The displacement trajectory and the vibration frequency at  $KC = 30$ ,  $U_r = 8$ .

( $f_n D / U_m$ ), while the transverse dominant frequency is always close to the natural frequency. With the increase of KC number, the oscillatory flow frequency becomes smaller and hence the reduction of streamwise dominant frequency. Nevertheless, both the streamwise and transverse dominant frequencies experience slight fluctuations over time, due to the competition among multiple frequencies. As shown in Fig. 12, in the constant KC number, with the increase of reduced velocity, the dominant frequency becomes closer to the natural frequency, while the secondary frequency is always near the natural frequency. At the same reduced velocity, the dominant frequency becomes smaller and smaller with the increase of KC number.

It can be seen from Fig. 13 that in the constant KC number, the vibration frequency of the transverse direction will also decrease with the reduced velocity decreasing. Except that when  $U_r = 3$ , the transverse vibration frequency is near the natural frequency and does not coincide with the natural frequency. In other cases, the transverse vibration frequency basically coincides with the natural frequency, which is similar to the situation described in Fig. 11.

The cylinder motion generates a relative velocity between the cylinder and ambient fluid. Therefore, the effective flow velocity  $U_R$  can be calculated by:

$$U_R = U_m \sin(2\pi t / T) - dX/dt \quad (8)$$

The amplitude of  $U_R$  is defined as  $U_{Rm}$ . Based on the maximum effective flow velocity ( $U_{Rm}$ ), the maximum effective KC number ( $KC_m$ )

is defined as:

$$KC_m = U_{Rm} T / D \quad (9)$$

It is seen from Fig. 14 that  $KC_m$  generally increases with  $U_r$ , due to the enlarged streamwise amplitude.

### 3.4. Oscillating trajectory

Dragomiretskiy and Zosso (2013) proposed a new completely non-recursive variation pattern decomposition (VMD) method. In this method, the modal decomposition is transformed into a variable decomposition problem and optimized by the alternate direction multiplier method. In the optimization process, the mode set of band-limited features is obtained. VMD is essentially an adaptive Wiener filter bank. It can separate modes with different central frequencies.

The constrained variation model is constructed as follows:

$$\left\{ \begin{array}{l} \min_{\{u_k\}, \{\omega_k\}} \left\{ \sum_k \left\| \theta_t \left[ \left( \delta(t) + \frac{j}{\pi t} \right) * u_k(t) \right] e^{-j\omega_k t} \right\|^2 \right\} \\ \text{s.t. } \sum_k u_k = f \end{array} \right\} \quad (10)$$

where,  $u_k$  represents each modal component;  $\omega_k$  is the center frequency;  $f$  is the original signal;  $*$  is the symbol of the convolution operation.

In order to obtain the optimal solution of the variation constraint

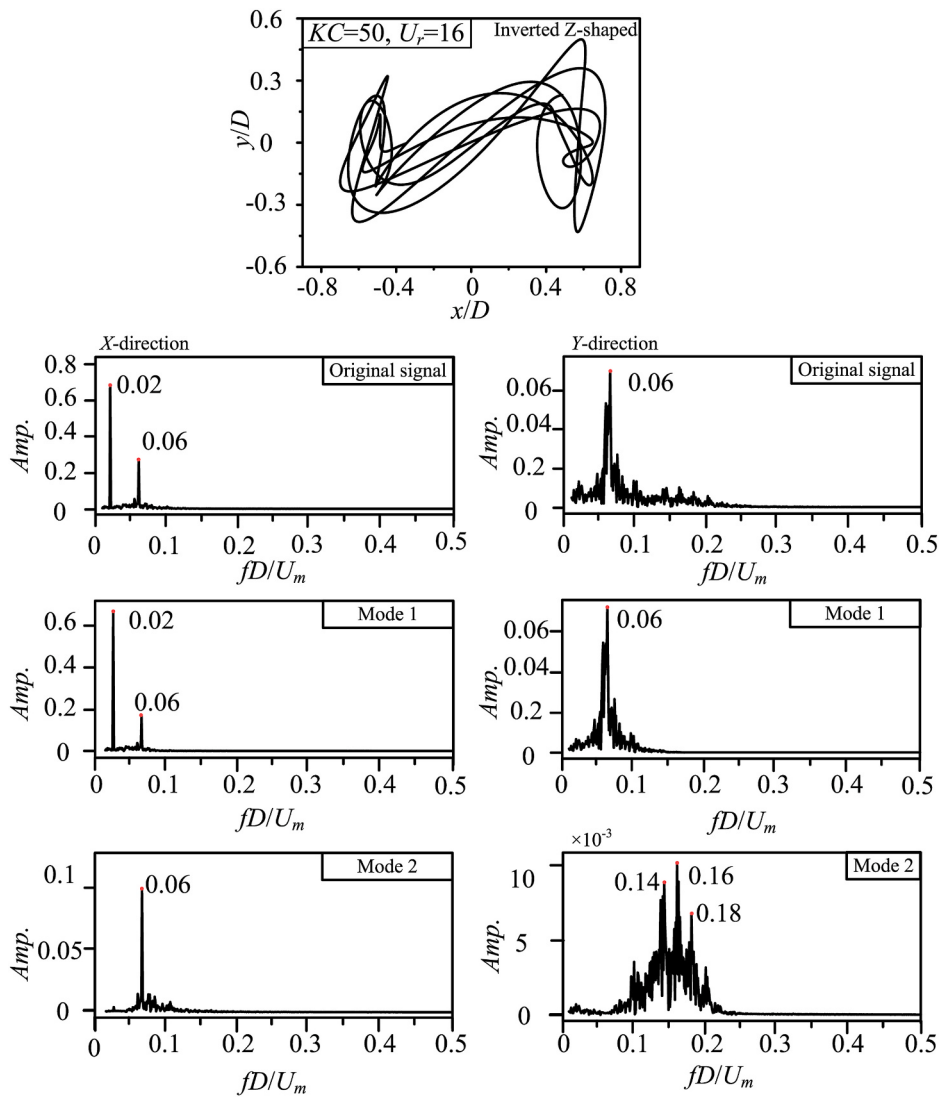


**Fig. 18.** The displacement trajectory and the vibration frequency at  $KC = 50$ ,  $U_r = 16$ .

model, quadratic penalty factor  $\alpha$  and Lagrange multiplication operator  $\lambda(t)$  are introduced to transform the constrained variation problem into an unconstrained variation solution problem. The extended Lagrange expression obtained is as follows:

$$\begin{aligned} L(\{u_k\}, \{\omega_k\}, \lambda(t)) = & \alpha \sum_k \left\| \partial_t \left[ \left( \delta(t) + \frac{j}{\pi t} \right) * u_k(t) \right] e^{-j\omega_k t} \right\|_2^2 \\ & + \left\| f(t) - \sum_k u_k(t) \right\|_2^2 + \langle \lambda(t), f(t) - \sum_k u_k(t) \rangle \end{aligned} \quad (11)$$

Then the alternating direction multiplier method is used to solve the variation problem, and the optimal solution of (11) is obtained by formula (12), (13), (14) iteratively updated  $u_k^{n+1}$ ,  $\omega_k^{n+1}$ ,  $\lambda^{n+1}$ . The iterative update expression is as follows:

$$u_k^{n+1}(\omega) = \frac{f(\omega) - \sum_{i=1, i \neq k}^K u_k(\omega) + \frac{\lambda(\omega)}{2}}{1 + 2\alpha(\omega - \omega_k)^2} \quad (12)$$

$$\omega_k^{n+1} = \frac{\int_0^\infty \omega |u_k(\omega)|^2 d\omega}{\int_0^\infty |u_k(\omega)|^2 d\omega} \quad (13)$$

$$\lambda_k^{n+1}(\omega) = \lambda^n(\omega) + \tau \left( f(\omega) - \sum_{k=1}^K u_k^{n+1}(\omega) \right) \quad (14)$$

where  $\tau$  is the noise tolerance parameter;  $n$  is the number of iterations;  $f(\omega)$ ,  $u_i(\omega)$ ,  $\lambda(\omega)$  and  $u_k^{n+1}(\omega)$  represent the Fourier transforms of the  $f(t)$ ,  $u_i(t)$ ,  $\lambda(t)$  and  $u_k^{n+1}(t)$ , respectively.

Until the iteration stop condition is satisfied, as shown in formula (15), the variational solution process ends and  $K$  modal components with finite bandwidth are obtained.

$$\frac{\sum_{k=1}^K \|u_k^{n+1} - u_k^n\|_2^2}{\|u_k^n\|_2^2} < \epsilon \quad (15)$$

where  $\epsilon$  is the judgment accuracy.

The VMD method overcomes the problems of Empirical Mode Decomposition (EMD) and aliasing of modal components and has a more solid mathematical theoretical foundation. It can reduce the non-stationarity of time series with high complexity and strong nonlinear and obtain relatively stable subsequences containing multiple different frequency scales, which is suitable for non-stationary sequences.

Fig. 15(a) shows the division of the displacement trajectory of all

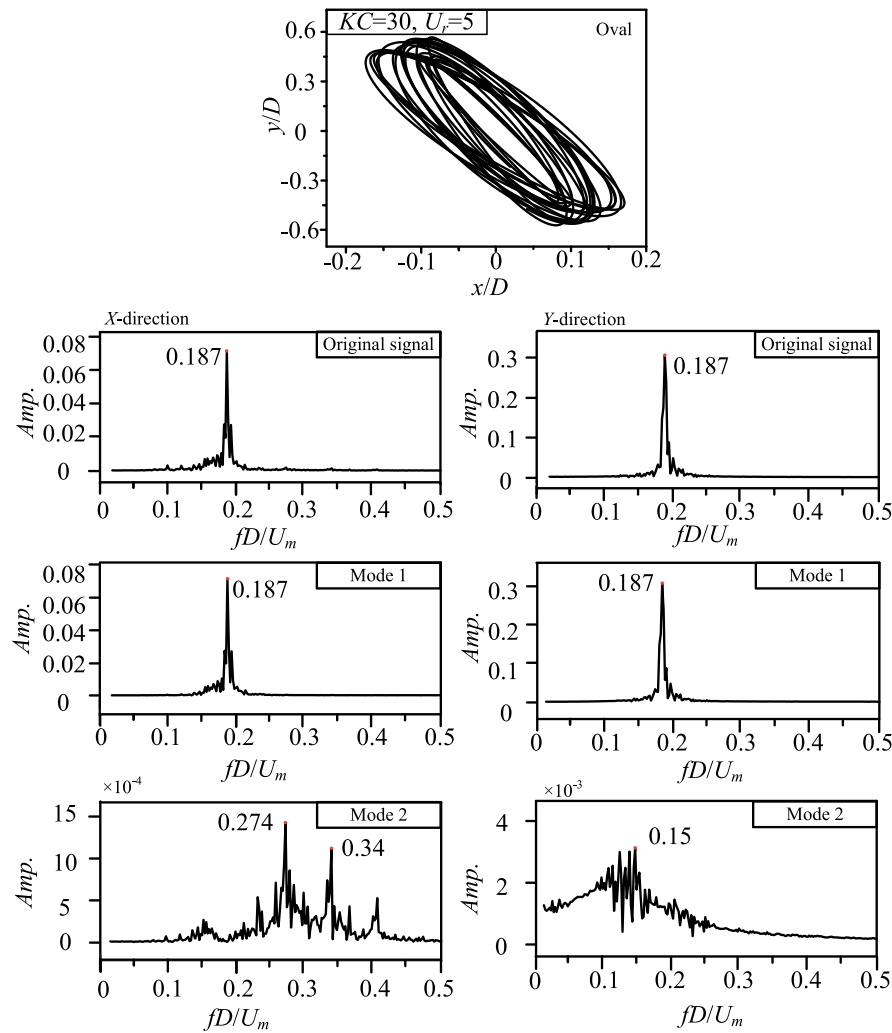


**Fig. 19.** The displacement trajectory and the vibration frequency at  $KC = 30$ ,  $U_r = 5$ .

groups, which can be divided into five types, namely Spiral, Cluttered, Oval, Inverted Z-shaped, and 8-shaped. The Spiral mainly appears in the low reduced velocity, the Cluttered mainly appears in the range of  $U_r$  from 7 to 14, and the Oval appears in the case of  $KC = 20$ ,  $U_r = 16$  and  $KC = 30$ ,  $U_r = 5$ , but not in the case of  $KC = 50$ . The inverted Z-shaped only appears in the case of  $KC = 20$ ,  $KC = 50$  at high reduced velocity, while the 8-shaped is mainly distributed in the case of  $KC = 20$ ,  $U_r = 10$  and  $KC = 30$ ,  $U_r = 13\text{--}16$ . Fig. 15 (b) shows the five types of representative shapes.

Figs. 16, 17, 18, 19 and 20 show the typical cases in the five displacement trajectories. The original modes of vibration frequency and the first and second modes after VMD mode decomposition are given.

As can be seen from Fig. 16, the displacement trajectory presents a Spiral shape when  $KC = 20$  and  $U_r = 3$ . The streamwise direction response has a dominant frequency and a secondary frequency, and the ratio of the dominant frequency is  $f_{xd}/f_{yd} = 1/6$ . Due to the sub-frequency of vibration, the displacement trajectories are deviated, and multiple displacement trajectories appear.

As can be seen from Fig. 17, when  $KC = 30$  and  $U_r = 8$ , there are many miscellaneous vortices. The shed vortices collide with the cylinder surface, resulting in the split and reattachment of vortices and hence the appearance of multiple frequencies. The transverse frequency is not an integral multiple of the streamwise frequency. Consequently, the oscillation trajectory becomes irregular.

It can be seen from Fig. 18 that when  $KC = 50$  and  $U_r = 16$ , the cylinder displacement trajectory is Inverted Z-shaped. The streamwise direction response has a dominant frequency and a secondary frequency, and the ratio of the dominant frequencies is  $f_{xd}/f_{yd} = 1/3$ .

It can be seen from Fig. 19 that when  $KC = 30$  and  $U_r = 5$ , the cylinder displacement trajectory presents an oval, and the frequency ratio of streamwise direction vibration transverse direction vibration is  $f_{xd}/f_{yd} = 1$ . According to the frequency after VMD decomposition, there are many sub-frequencies in the streamwise and transverse direction responses, which leads to the elliptic displacement trajectory in the oscillating flow is not as perfect as the oval displacement trajectory in the steady flow.

It can be seen from Fig. 20 that the cylinder displacement trajectory presents a shape of "8" when  $KC = 30$  and  $U_r = 16$ . At this time, the frequency ratio of streamwise direction vibration to transverse direction vibration is  $f_{xd}/f_{yd} = 1/2$ .

### 3.5. Wake structure

Fig. 21 (a) shows the division diagram of the end result after vortex shedding, which can be divided into four types, namely, Split, Merging, Split and Merging, and Dissipate. Because the oscillation period is small and the motion condition is variable, the four types all exist when  $KC = 20$ . For  $KC = 30$ , the Split and Merging form mainly exists in the low reduced velocity and high reduced velocity, while the Split mainly exists

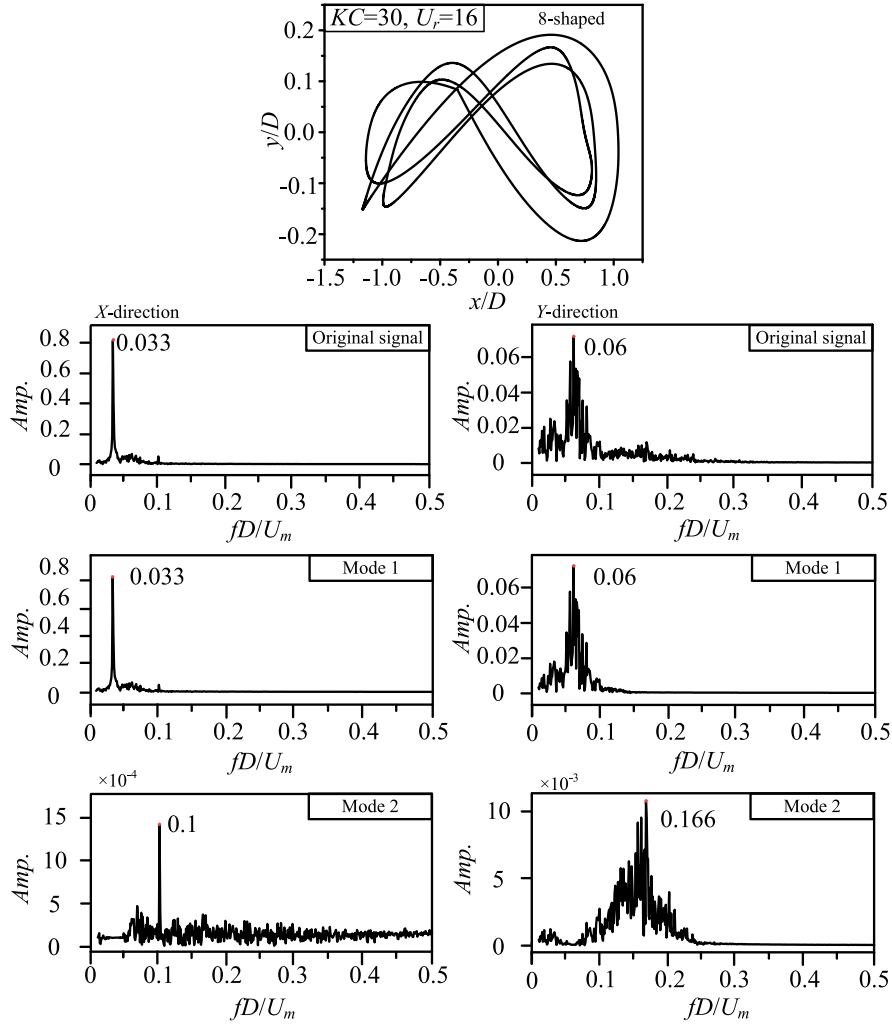


**Fig. 20.** The displacement trajectory and the vibration frequency at  $KC = 30$ ,  $U_r = 16$ .

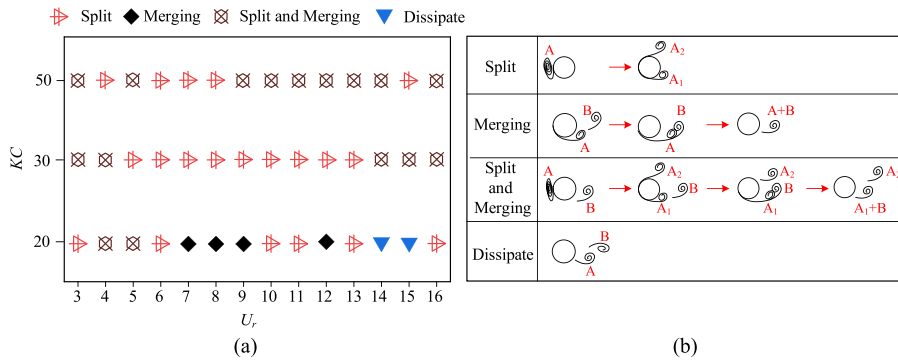


**Fig. 21.** The division of the incidence of vortex shedding.

in  $5 < U_r < 13$ . For  $KC = 50$ , Split and Merging exists in the majority.

Fig. 21 (b) shows a schematic diagram of these four types. Split means that after a vortex falls off in an oscillation period, it will strike the cylinder again when the velocity direction changes, resulting in the vortex being split into two parts by impact, one part reattaches to the surface of the cylinder and then falls off, and the other part directly dissipates. The Merging is that the vortex that has fallen off and the vortex that has not fallen off fuse together and fall off together in one

oscillation period. In a period of oscillation, the vortex experiences both Split and Merging. It may be that one vortex experiences split and merging, or it may be that one vortex experiences merging and another vortex experiences split. Dissipation is the occurrence of no split or merging and gradually dissipates after the vortex breaks away from the separation point.

Figs. 22–25 give the lift and drag coefficient curves along with time, and vorticity distribution at different moments in a cycle corresponding

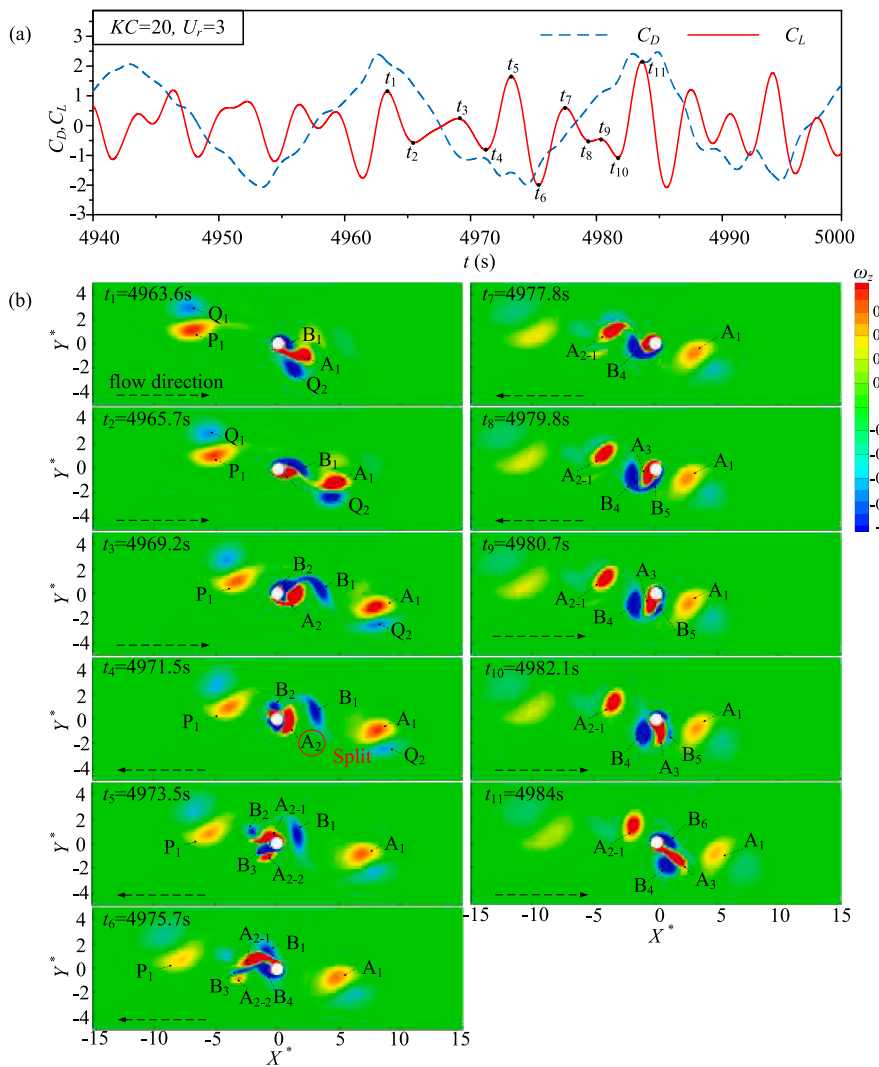


**Fig. 22.** Schematic diagram of vortex splitting in an oscillation period at  $KC = 20$ ,  $U_r = 3$ : (a) time histories of lift coefficients and drag coefficients; (b) the instantaneous evolution of vortices in one cycle.

to the typical groups of the four occurrences, respectively. The vorticity contours show that the generation, detachment, and development of vortices. The smaller the oscillation period, the faster the direction of fluid motion changes, which will make the newly detached vortex not have enough time to dissipate and some vortices will collide with the cylinder again. Meanwhile, the impact of the vortex also affects the vibration of the cylinder. In the figures, the  $A$  represents the vortex rotating clockwise in the current period,  $B$  represents the vortex rotating counterclockwise in the current period, and the subscript from 1 to  $n$  represents the first, and second, until the  $n$  vortices, respectively. The  $P$  and  $Q$  represent the vortices generated in the last period but not completely dissipated, where the letter  $P$  represents the vortices rotating clockwise in the last period, and the letter  $Q$  represents the vortices rotating counterclockwise in the last period, and the subscript numbers express the same meaning as above. As seen in Figs. 22–25, nine, four, thirteen and four vortices are formed in the wake in one oscillatory flow period, respectively, due to the split and merging of vortices. At a given KC number, the number of shed vortices generally reduces with the increase of reduced velocity, contributing to the reduction of transverse frequency.

As can be seen from Fig. 22, when  $KC = 20$  and  $U_r = 3$ , a vortex Split occurs. Fig. 22(a) represents the time-history curve of the lift resistance coefficient of  $KC = 20$  and  $U_r = 3$ . The moment corresponding to the

peak and trough on the time-history curve of the lift coefficient of an oscillation period is selected. Fig. 22(b) represents the vorticity cloud map corresponding to the time selected by Fig. 22(a). It can be seen that the vortex  $A_2$  falling off at the time  $t = 4971.5s$  moves along the velocity direction after changing and is divided into two parts after impacting the cylinder, with one part reattached to the surface of the cylinder and the other part gradually dissipating after falling off. and the other part falls off and dissipates gradually.

It can be seen from Fig. 23 that the vorticity merges when  $KC = 20$  and  $U_r = 9$ . Fig. 23 (a) represents the time-history curve of the lift resistance coefficient of  $KC = 20$  and  $U_r = 9$ . The moment corresponding to the peak and trough on the time-history curve of the lift coefficient of an oscillation period is selected. Fig. 23 (b) represents the vorticity cloud map corresponding to the time selected by Fig. 23 (a). It is found that the vortex  $Q_1$  generated in the last period merges with the vortex  $B_1$  in the current period at the time  $t = 4979s$ , while the newly generated vortex  $B_1+Q_1$  reattaches the cylinder surface at the time  $t = 4985.3s$  due to the change of velocity direction.

As can be seen from Fig. 24, when  $KC = 20$  and  $U_r = 3$ , the vorticity split and merges. Fig. 24 (a) represents the time-history curve of the lift and drag coefficient of  $KC = 50$  and  $U_r = 3$ . The moment corresponding to the peak and trough of the time-history curve of the lift coefficient of an oscillation period is selected. Fig. 24 (b) represents the vorticity cloud

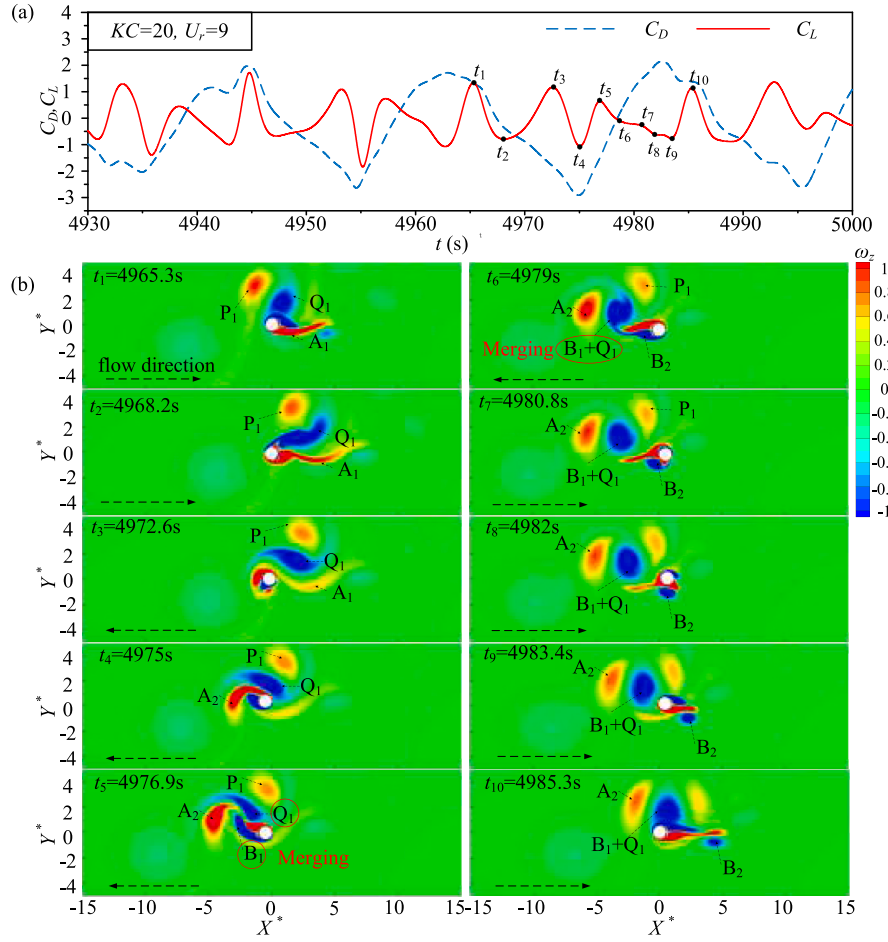


**Fig. 23.** Schematic diagram of vortex splitting in an oscillation period at  $KC = 20$ ,  $U_r = 9$ : (a) time histories of lift coefficients and drag coefficients; (b) the instantaneous evolution of vortices in one cycle.

map corresponding to the time selected by Fig. 21 (a). It is found that when  $t = 5004$ s, vortex  $A_4$  merges with vortex  $A_5$  after falling off due to the change of velocity direction. When the velocity direction of  $A_7$  changes at  $t = 5031$ s, the vortex moves along the velocity direction and is divided into two parts after striking the cylinder, one part reattaches to the surface of the cylinder, and the other part falls off and dissipates gradually.

As can be seen from Fig. 25, the vortex does not appear Split, Merging, Split and Merging, that is, Dissipate when  $KC = 20$  and  $U_r = 3$ . Fig. 25 (a) represents the time-history curve of the lift resistance coefficient of  $KC = 20$  and  $U_r = 14$ . The time corresponding to the peak and trough of the time-history curve of the lift coefficient of an oscillation period is selected. Fig. 25 (b) represents the vorticity cloud map corresponding to the selected time of Fig. 25 (a). It is found that the vorticity did not split and merge during the selected oscillation period, but gradually dissipated after falling off.

#### 4. Conclusions

Two-degree-of-freedom VIV of a circular cylinder in oscillatory flow is numerically investigated in this work. Simulations are carried out at  $Re = 150$ ,  $\zeta = 0$ ,  $m^* = 10$ ,  $KC = 20, 30$ , and  $50$ , and reduced velocity from 3 to 16. The vibration amplitude, hydrodynamics forces on the cylinder, and the vortex shedding mode are discussed. The conclusions are summarized as follows.

- (1) For each  $KC$  number, the variations of the RMS streamwise and the RMS transverse force coefficients with the reduced velocity are characterized by rapidly increasing to a peak followed by gradually decreasing and then stable with the increase of reduced velocity. The variation of the root mean square (RMS) force coefficient is similar to the changes in the transverse amplitude with the reduced velocity. Due to the separation of the shear layer, the averaged pressure curve of each stage presents an obvious V-shape within the range of  $0 \leq \alpha \leq 180^\circ$ . The minimum averaged pressure coefficients of different  $KCs$  number also decrease with the increase of reduced velocity. The greater the reduced velocity, the more obvious the difference between the averaged pressure coefficients of the three  $KCs$  number. When the velocity direction changes, the distribution of positive and negative pressure also changes. In the  $0.5T$  including the change of velocity direction, the distribution of positive and negative pressure presents a center symmetry with the change of velocity. The averaged pressure coefficient is 0 at the front and rear stagnation points of the cylinder, presenting a V-shaped at  $0 \leq \alpha \leq 180^\circ$  and W-shaped at  $0 \leq \alpha \leq 360^\circ$ .
- (2) The larger the  $KC$  number, the smaller the streamwise amplitude. The cycle of oscillating flow becomes larger with the growth of  $KC$  number, contributing to more stable movement of the cylinder and hence the reduction of streamwise amplitude. By comparing the frequency amplitude with the natural frequency of different  $KC$  number and giving the wavelet spectrum in the XY-directions at the different  $KC$  number and reduced velocity, it can

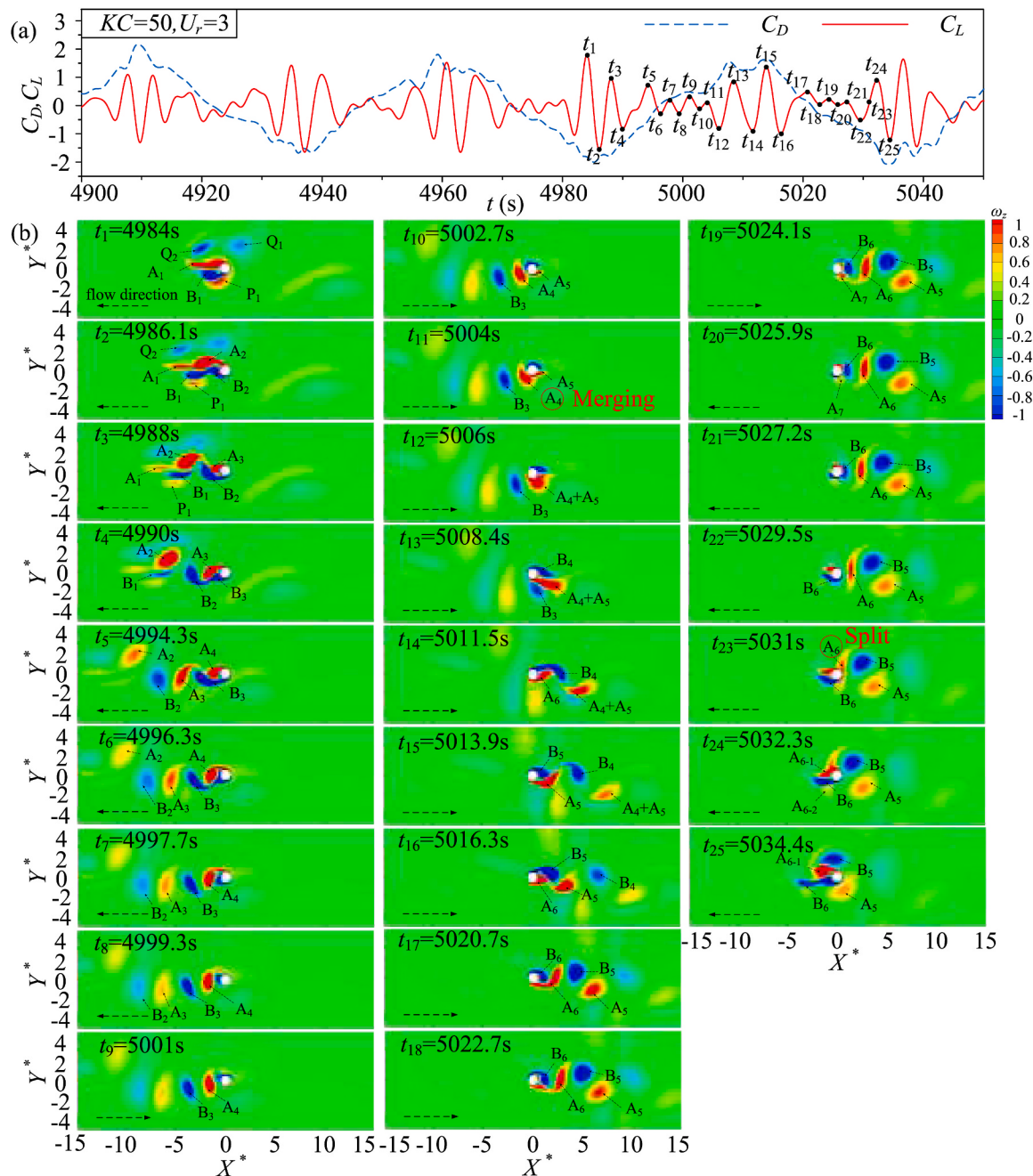


**Fig. 24.** Schematic diagram of vortex splitting in an oscillation period at  $KC = 50$ ,  $U_r = 3$ : (a) time histories of lift coefficients and drag coefficients; (b) the instantaneous evolution of vortices in one cycle.

be seen that the streamwise dominant frequency does not coincide with the natural frequency of the cylinder, while the transverse dominant frequency is always close to the natural frequency. With the increase of KC number, the oscillatory flow frequency becomes smaller and hence the reduction of streamwise dominant frequency. Nevertheless, both the streamwise and transverse dominant frequencies experience slight fluctuations over time, due to the competition among multiple frequencies.

- (3) The VMD mode decomposition of vibration displacement is carried out. The results show that the displacement trajectory can be divided into five types, namely Spiral, Chaos, Oval, Inverted Z-shaped and 8-shaped.
- (4) The fate of the vortex after the vortex falls off is divided into four types, including Split, Merging, Split and Merging, and Dissipate.

Because the oscillation period is small and the motion condition is changeable, the four types of  $KC = 20$  are preserved. For  $KC = 30$ , the Split and Merging form mainly exists in the low and high reduced velocities, while the Split mainly exists in the  $U_r$  range of 5–13. For  $KC = 50$ , Split and Merging exists in the majority. This rule only applies to the case where the vibration is regular and repeatable.

#### CRediT authorship contribution statement

**Hongjun Zhu:** Writing – review & editing, Supervision, Resources, Methodology, Conceptualization. **Huifen Xu:** Writing – original draft, Formal analysis. **Bin Liu:** Writing – review & editing. **Jiawen Zhong:** Writing – review & editing.

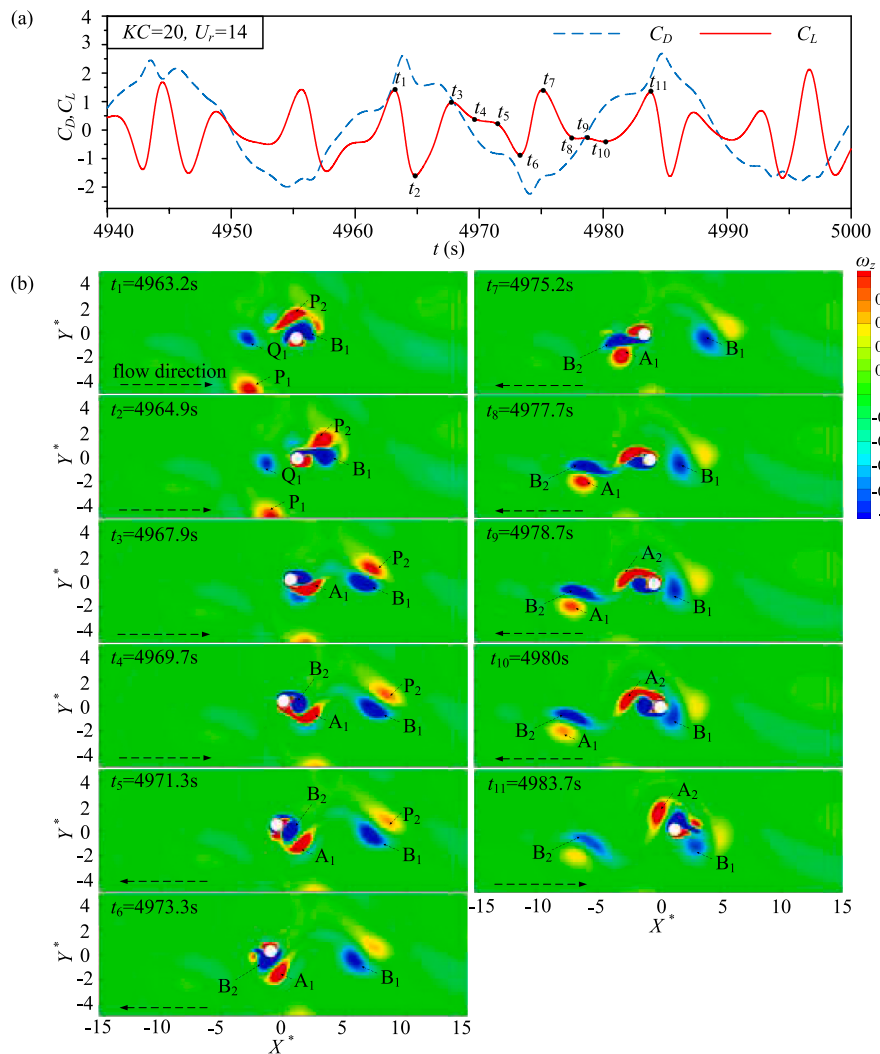


**Fig. 25.** Schematic diagram of vortex splitting in an oscillation period at  $KC = 20$ ,  $U_r = 14$ : (a) time histories of lift coefficients and drag coefficients; (b) the instantaneous evolution of vortices in one cycle.

#### Declaration of competing interest

The authors declare that they have no known competing financial interests or personal relationships that could have appeared to influence the work reported in this paper.

#### Acknowledgements

The research work was supported by National Natural Science Foundation of China (Nos. 51979238 and 52301338) and Sichuan Science and Technology Program (Nos. 2023NSFSC1953 and 2023ZYD0140). The authors appreciate the support from the Offshore Oil and Gas Laboratory at Southwest Petroleum University.

#### Appendix A. Supplementary data

Supplementary data to this article can be found online at <https://doi.org/10.1016/j.oceaneng.2024.118666>.

#### References

- An, H., Cheng, L., Zhao, M., 2015. Two-dimensional and three-dimensional simulations of oscillatory flow around a circular cylinder. *Ocean Eng.* 109, 270–286.
- Anagnostopoulos, P., Iliadis, G., 1998. Numerical study of the flow pattern and the in-line response of a flexible cylinder in an oscillating stream. *J. Fluid Struct.* 12 (3), 225–258.
- Bearman, P.W., Currie, I.G., 1979. Pressure-fluctuation measurements on an oscillating circular cylinder. *J. Fluid Mech.* 91 (4), 661–677.
- Brika, D., Laneville, A., 1999. The flow interaction between a stationary cylinder and a downstream flexible cylinder. *J. Fluid Struct.* 13 (5), 579–606.
- Carberry, J., Govardhan, R., Sheridan, J., Rockwell, D., Williamson, C.H., 2004. Wake states and response branches of forced and freely oscillating cylinders. *Eur. J. Mech. B Fluid* 23 (1), 89–97.
- Carberry, J., Sheridan, J., Rockwell, D., 2005. Controlled oscillations of a cylinder: forces and wake modes. *J. Fluid Mech.* 558, 31–69.
- Chung, M.H., 2016. Two-degree-of-freedom vortex induced vibration of low-mass horizontal circular cylinder near a free surface at low Reynolds number. *Int. J. Heat Fluid Flow* 57, 58–78.
- Dragomireski, K., Zosso, D., 2013. Variational mode decomposition. *IEEE Trans. Signal Process.* 62 (3), 531–544.
- Elston, J.R., Blackburn, H.M., Sheridan, J., 2006. The primary and secondary instabilities of flow generated by an oscillating circular cylinder. *J. Fluid Mech.* 550, 359–389.
- Feng, C.C., 1968. The Measurement of Vortex Induced Effects in Flow Past Stationary and Oscillating Circular and D-Section Cylinders. Doctoral dissertation, University of British Columbia.
- Gopalakrishnan, R., 1993. Vortex-induced Forces on Oscillating Bluff Cylinders. Doctoral dissertation, Massachusetts Institute of Technology.
- Henderson, R.D., 1997. Nonlinear dynamics and pattern formation in turbulent wake transition. *J. Fluid Mech.* 352, 65–112.
- Honji, H., 1981. Streaked flow around an oscillating circular cylinder. *J. Fluid Mech.* 107, 509–520.
- Hover, F.S., Davis, J.T., Trianafyllou, M.S., 2004. Three-dimensionality of mode transition in vortex-induced vibrations of a circular cylinder. *Eur. J. Mech. B Fluid* 23 (1), 29–40.

- Jiang, H., Cheng, L., Draper, S., An, H., Tong, F., 2016. Three-dimensional direct numerical simulation of wake transitions of a circular cylinder. *J. Fluid Mech.* 801, 353–391.
- Justesen, P., 1991. A numerical study of oscillating flow around a circular cylinder. *J. Fluid Mech.* 222, 157–196.
- Kang, Z., Ni, W., Sun, L., 2016. An experimental investigation of two-degrees-of-freedom VIV trajectories of a cylinder at different scales and natural frequency ratios. *Ocean Eng.* 126, 187–202.
- Khalak, A., Williamson, C.H., 1997. Investigation of relative effects of mass and damping in vortex-induced vibration of a circular cylinder. *J. Wind Eng. Ind. Aerod.* 69, 341–350.
- Kozakiewicz, A., Sumer, B.M., Fredsøe, J., 1994. Cross-flow vibrations of cylinder in irregular oscillatory flow. *J. Waterw., Port, C-ASCE* 120 (6), 515–534.
- Kozakiewicz, A., Sumer, B.M., Fredsøe, J., 1992. Spanwise correlation on a vibrating cylinder near a wall in oscillatory flows. *J. Fluid Struct.* 6 (3), 371–392.
- Kozakiewicz, A., Sumer, B.M., Fredsøe, J., Hansen, E.A., 1997. Vortex regimes around a freely vibrating cylinder in oscillatory flow. *Int. J. Offshore Polar* 7 (2), 94–103.
- Lam, K.M., Hu, J.C., Liu, P., 2010. Vortex formation processes from an oscillating circular cylinder at high Keulegan-Carpenter numbers. *Phys. Fluids* 22 (1), 1–14.
- Lipsett, A.W., Williamson, I.D., 1994. Response of a cylinder in oscillatory flow. *J. Fluid Struct.* 8 (7), 681–709.
- Moe, G., Wu, Z., 1990. The lift force on a cylinder vibrating in a current. *Offshore Mech. Arct. Engage* 112 (4), 297–303.
- Morse, T.L., Williamson, C.H.K., 2006. Employing controlled vibrations to predict fluid forces on a cylinder undergoing vortex-induced vibration. *J. Fluid Struct.* 22 (6–7), 877–884.
- Obasaju, E.D., Bearman, P.W., Graham, J.M.R., 1988. A study of forces, circulation and vortex patterns around a circular cylinder in oscillating flow. *J. Fluid Mech.* 196, 467–494.
- Pan, Z.Y., Cui, W.C., Zhang, X.C., 2005. Overview on VIV of slender marine structures. *J. Ship Mech.* 9 (6), 135–154.
- Patrikalakis, N.M., Chryssostomidis, C., 1986. Vortex-induced response of a flexible cylinder in a sheared current. *Energy Resour. Technol.* 108 (1), 59–64.
- Sarpkaya, T., 1986. Force on a circular cylinder in viscous oscillatory flow at low Keulegan-Carpenter numbers. *J. Fluid Mech.* 165, 61–71.
- Sarpkaya, T., 2004. A critical review of the intrinsic nature of vortex-induced vibrations. *J. Fluid Struct.* 19 (4), 389–447.
- Singh, S.P., Mittal, S., 2005. Vortex-induced oscillations at low Reynolds numbers: hysteresis and vortex-shedding modes. *J. Fluid Struct.* 20 (8), 1085–1104.
- Staubli, T., 1983. Calculation of the vibration of an elastically mounted cylinder using experimental data from forced oscillation. *Fluids Eng* 105 (2), 225–229.
- Sumer, B.M., Fredsøe, J., 1988. Transverse vibrations of an elastically mounted cylinder exposed to an oscillating flow. *J. Offshore Mech. Arct.* 110 (4), 387–394.
- Sumer, B.M., Fredsøe, J., Jensen, K., 1994. A note on spanwise correlation on a freely vibrating cylinder in oscillatory flow. *J. Fluid Struct.* 8 (3), 231–238.
- Taheri, E., Zhao, M., Wu, H., 2022. Numerical investigation of the vibration of a circular cylinder in oscillatory flow in oblique directions. *J. Mar. Sci. Eng.* 10 (6), 767.
- Taheri, E., Zhao, M., Wu, H., Tong, F., 2020. Numerical investigation of streamwise vibration of an elastically mounted circular cylinder in oscillatory flow. *Ocean Eng.* 209, 107300.
- Tatsuno, M., Bearman, P.W., 1990. A visual study of the flow around an oscillating circular cylinder at low Keulegan-Carpenter numbers and low Stokes numbers. *J. Fluid Mech.* 211, 157–182.
- Wang, H., Ding, L., Zhang, L., Zou, Q., Wu, C., 2019. Control of two-degree-of-freedom vortex-induced vibrations of a circular cylinder using a pair of synthetic jets at low Reynolds number: influence of position angle and momentum coefficient. *Int. J. Heat Fluid Flow* 80, 108490.
- Williamson, C.H., 1996. Vortex dynamics in the cylinder wake. *Annu. Rev. Fluid Mech.* 28 (1), 477–539.
- Williamson, C.H.K., 1985. Sinusoidal flow relative to circular cylinders. *J. Fluid Mech.* 155, 141–174.
- Williamson, C.H.K., Govardhan, R., 2008. A brief review of recent results in vortex-induced vibrations. *J. Wind Eng. Ind. Aerod.* 96 (6–7), 713–735.
- Williamson, C.H., Govardhan, R., 2004. Vortex-induced vibrations. *Annu. Rev. Fluid Mech.* 36, 413–455.
- Zhao, M., 2013. Numerical investigation of two-degree-of-freedom vortex-induced vibration of a circular cylinder in oscillatory flow. *J. Fluid Struct.* 39, 41–59.
- Zhao, M., Cheng, L., An, H., 2012. Numerical investigation of vortex-induced vibration of a circular cylinder in transverse direction in oscillatory flow. *Ocean Eng.* 41, 39–52.
- Zhao, M., Kaja, K., Xiang, Y., Yan, G., 2013. Vortex-induced vibration (VIV) of a circular cylinder in combined steady and oscillatory flow. *Ocean Eng.* 73, 83–95.